J. Fluid Mech. (2025), *vol.* 1015, A21, doi:10.1017/jfm.2025.10326

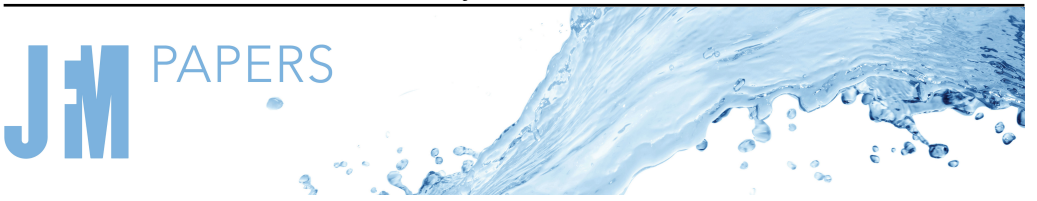

Effects of settling on inertial particle slip velocity statistics in wall-bounded flows

Andrew P. Grace[1], **Tim Berk**[2], **Andrew D. Bragg**[3] and **David H. Richter**[1]

[1]Department of Civil and Environmental Engineering and Earth Sciences, University of Notre Dame, Notre Dame, IN 46556, USA

[2]Department of Mechanical and Aerospace Engineering, Utah State University, Logan, UT 84322, USA

[3]Department of Civil and Environmental Engineering, Duke University, Durham, NC 27708, USA

Corresponding author: Andrew P. Grace, agrace4@nd.edu

(Received 19 June 2024; revised 3 March 2025; accepted 12 April 2025)

Developing reduced-order models for the transport of solid particles in turbulence typically requires a statistical description of the particle–turbulence interactions. In this work, we utilize a statistical framework to derive continuum equations for the moments of the slip velocity of inertial, settling Lagrangian particles in a turbulent boundary layer. Using coupled Eulerian–Lagrangian direct numerical simulations, we then identify the dominant mechanisms controlling the slip velocity variance, and find that for a range of Stokes number St^+, Settling number Sv^+ and Reynolds number Re_τ (based on frictional scales), the slip variance is primarily controlled by local differences between the 'seen' variance and the particle velocity variance, while terms appearing due to the inhomogeneity of the turbulence are subleading until Sv^+ becomes large. We also consider several comparative metrics to assess the relative magnitudes of the fluctuating slip velocity and the mean slip velocity, and we find that the vertical mean slip increases rapidly with Sv^+, rendering the variance relatively small – an effect found to be most substantial for $Sv^+ > 1$. Finally, we compare the results with a model of the acceleration variance (Berk & Coletti 2021 *J. Fluid Mech.* **917**, A47) based the concept of a response function described in Csanady (1963 *J. Atmos. Sci.* **20**, 201–208), highlighting the role of the crossing trajectories mechanism. We find that while there is good agreement for low Sv^+, systematic errors remain, possibly due to implicit non-local effects arising from rapid particle settling and inhomogeneous turbulence. We conclude with a discussion of the implications of this work for modelling the transport of coarse dust grains in the atmospheric surface layer.

Key words: multiphase flow, particle/fluid flow, Navier–Stokes equations

1. Introduction

The study of the transport of inertial particles through fluids finds numerous applications in the natural sciences and in industry. A significant focus is placed on understanding how small but heavy particles respond to turbulence processes, and how to model these processes in a physically coherent way. One such example is understanding the global transport of coarse dust particles (30–100 μm) once they are emitted from the surfaces of arid regions (Rosenberg *et al.* 2014; Meng *et al.* 2022; Adebiyi *et al.* 2023; Kok *et al.* 2023). These particles can be lofted high into the turbulent atmosphere where they can be transported many hundreds to thousands of kilometres depending on their size (Shao 2008; Van Der Does *et al.* 2018). The interactions between the dust particles and the carrier phase must be parameterized since such interactions occur at the particle scale, and cannot be represented explicitly due to unrealistic computational requirements. Understanding the impacts of turbulence on particle transport characteristics, such as emission and deposition (Kok *et al.* 2012), will help us to understand their overall role in global climate processes (Kok 2011; Ryder *et al.* 2019; Kok *et al.* 2023), biogeochemical cycles (Ryder *et al.* 2018) and human health.

From a dynamical perspective, solid particles are subjected to various forces as they travel through a turbulent flow. For small (relative to the local Kolmogorov scale) and dense (relative to the carrier phase) spherical particles, the most important forces are due to gravity and hydrodynamic drag (Maxey & Riley 1983). Since the seminal work of Wang & Stock (1993), there has been a significant push to try to understand how gravity and turbulent drag couple together to affect both mean and fluctuating quantities through experiment and simulation (Aliseda *et al.* 2002; Good *et al.* 2014; Rosa *et al.* 2016; Tom & Bragg 2019; Mora *et al.* 2021; Ferran *et al.* 2023). Importantly, in a turbulent flow, the bias created by gravity leads to a more rapid decorrelation of the turbulence along particle trajectories, meaning that there is an implicit and nonlinear coupling between gravity and turbulent drag, resulting in a fundamental change in the forcing induced by the turbulence. This is an example of the crossing trajectories effect (Yudine 1959; Csanady 1963). Crossing trajectories occurs when Lagrangian particle trajectories cross fluid particle trajectories due to mean Lagrangian particle drift (which can occur even in the absence of turbulence). The net effect is that Lagrangian particles may experience higher frequency fluid fluctuations leading to an increase in the particle dispersion. Crossing trajectories has also been shown to increase the horizontal and vertical components of particle acceleration variance in simulations of settling Lagrangian point particles in homogeneous isotropic turbulence (HIT) (Ireland, Bragg & Collins 2016*b*), in numerical simulations of turbulent boundary layers (TBL) (Lavezzo *et al.* 2010) as well as laboratory experiments in both set-ups (Gerashchenko *et al.* 2008; Berk & Coletti 2021). The turbulent drag is often quantified via the particle slip velocity, which is the difference between the fluid velocity seen by the particle, and the particle's velocity. Understanding the controlling mechanisms of the particle slip velocity and their magnitude within wall-bounded turbulence is key for estimating the particle Reynolds number (Balachandar 2009), as well building physically coherent stochastic dispersion models for Reynolds-averaged Navier–Stokes (Arcen & Tanière 2009) applications.

In this work, we are particularly focused on understanding the dynamic regimes characteristic of coarse dust particles in the Earth's atmospheric surface layer (the lowest 100 m of the Earth's atmosphere). Specifically, we consider how gravitational acceleration implicitly modifies the mechanisms controlling the particle slip velocity in a TBL. In a TBL, turbulence is driven by fluid shear originating at the solid lower boundary, resulting

in turbulence inhomogeneity and a height dependence of the parameters governing both the turbulent flow and the particle transport. Dynamically, a TBL is characterized by a very thin laminar sublayer where viscosity plays a dominant role, followed by a smooth transitional layer, known as the buffer layer, to a layer where viscous effects become negligible, known as the logarithmic layer. A review of TBLs can be found in Smits, McKeon & Marusic (2011).

Many studies of particle transport in TBLs tend to ignore the impact of gravitational acceleration *a priori* in an attempt to try to decouple the effects of turbulent drag and gravity (Marchioli *et al.* 2008; Balachandar 2009; Zamansky, Vinkovic & Gorokhovski 2011; Johnson, Bassenne & Moin 2020). However, due to the implicit coupling between gravity and turbulent drag, we must take care when extrapolating results from studies without gravity to those with gravity (Brandt & Coletti 2022). Furthermore, much of our understanding of particle-laden flows under the influence of gravitational settling comes from numerical (Bec, Homann & Ray 2014; Good *et al.* 2014; Ireland *et al.* 2016*b*; Tom & Bragg 2019) or laboratory (Aliseda *et al.* 2002; Mora *et al.* 2021; Ferran *et al.* 2023) configurations of HIT, due to the relative simplicity of the set-up. There are a few studies aiming to understand the statistical behaviour of settling inertial particles in TBLs (Lavezzo *et al.* 2010; Lee & Lee 2019; Berk & Coletti 2020; Bragg, Richter & Wang 2021*a*,*b*; Berk & Coletti 2023), and while they are far less numerous, they indicate the potential for gravitational settling to modify the dynamics of particle settling and two-way coupling due to the presence of the solid boundary. Indeed, Bragg *et al.* (2021*b*) showed that gravitational settling can have a strong impact on the particle transport in a TBL even for very small settling numbers for which is has been traditionally assumed that the effect of settling should be negligible. Having quantitative evidence as to when we may apply models designed under the assumptions of homogeneous turbulence to dynamics in a TBL, and when the settling is important for the particle transport, would be a useful starting point when designing a more unified theory.

In the following work, our goals are:

(i) to derive continuum equations for moments of the particle slip velocity and identify the leading-order balance of the variance throughout the TBL;
(ii) to determine the parametric conditions under which the slip velocity is governed by its mean component, fluctuating component or some combination of both;
(iii) to compare the results from the direct numerical simulations (DNS) in a TBL with a model based on the response function in homogeneous turbulence approach outlined in Csanady (1963) and Berk & Coletti (2021), and identify potential discrepancies;
(iv) to discuss implications for the transport of coarse particles in the atmospheric surface layer.

Section 2 provides the technical background on the carrier and particle phase equations as well as the governing parameters. We also derive the diagnostic equation for the vertical component of the slip velocity variance and discuss the model hierarchy. We choose to focus on the slip velocity variance specifically for several reasons. First, accurate estimates of the particle Reynolds number rely on the estimates of the magnitude of the slip velocity, and this quantity is not easily accessible in a laboratory or field setting directly. Second, it is related to the particle acceleration variance, which gives us a clue as to how the particles respond to turbulent structures within the flow. Section 3 presents the results of the study, while § 4 summarizes and provides a discussion on how the results relate to coarse dust transport in the atmospheric surface layer.

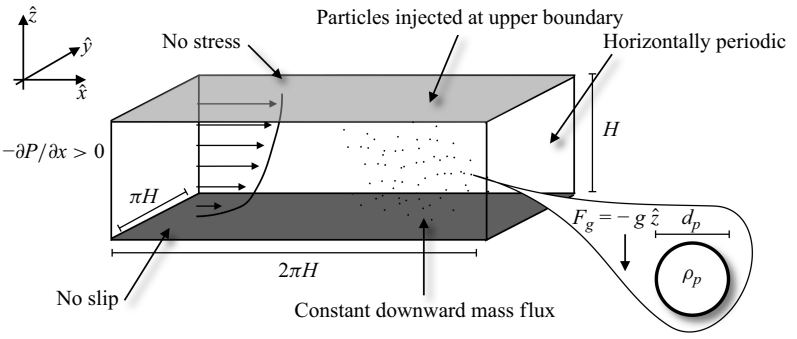

Figure 1. A schematic of the numerical set-up. The domain is a rectangular channel of height H, streamwise length $2\pi H$ and spanwise width πH. The flow is periodic in the horizontal and is driven by a constant pressure gradient in the streamwise direction, while the no-stress and no-slip boundary conditions are enforced at the top and bottom boundaries, respectively. Particles are injected at the upper boundary at a random horizontal location with an initial velocity equal to the fluid velocity at their location and removed when they contact the bottom boundary. They are allowed to rebound elastically off the upper boundary.

2. Technical background

2.1. *Carrier phase*

In this work, we use the NCAR Turbulence with Lagrangian Particles Model (Richter & Chamecki 2018) to model one-way coupled inertial particles settling through a TBL. This code has been validated and used in multiple studies focused on inertial particle settling and transport in TBLs (Richter & Chamecki 2018; Wang *et al.* 2019; Bragg *et al.* 2021*a*; Gao, Samtaney & Richter 2023; Grace, Richter & Bragg 2024). For the carrier phase, we use DNS to solve the three-dimensional, incompressible Navier–Stokes equations in a turbulent open channel flow set-up,

$$\frac{D\boldsymbol{u}}{Dt} = -\frac{1}{\rho_a}\nabla p + \nu\nabla^2\boldsymbol{u} - \frac{1}{\rho_a}\frac{\mathrm{d}P}{\mathrm{d}x}\hat{\boldsymbol{x}}, \tag{2.1}$$

$$\nabla\cdot\boldsymbol{u} = 0. \tag{2.2}$$

A schematic of the set-up is presented in figure 1. In the above equations, D/Dt represents the material derivative, $\boldsymbol{u}$ represents the three-dimensional flow velocity, p represents the turbulent pressure field, ρ_a is the carrier phase density and ν is the kinematic viscosity. Unconditional fluid velocities will be referred to by their components (u, v, w) with no subscript, and fluctuating quantities will be denoted by a prime. For example, as we are primarily focused on wall normal motion in this work, we will refer to fluctuating vertical fluid velocities as w'. The code uses a pseudospectral method in the horizontal directions and a second-order finite difference method in the vertical. We have clustered points near the solid lower boundary using an algebraic grid stretching procedure, so that $\Delta z_1 = 0.8\nu/u_\tau$ (u_τ is the friction velocity, defined below), where Δz_1 is the first grid point and $(\Delta x_\eta, \Delta y_\eta, \Delta z_\eta) = (2.8, 1.4, 0.9)$ at the midplane of the flow, where the subscript η represents the grid spacing in terms of the local Kolmogorov scale, defined below.

At the lower boundary, a no-slip boundary condition is enforced, while at the upper boundary, a no-stress boundary condition ($\partial u/\partial z = \partial v/\partial z = 0$ at $z = H$) is enforced. The domain is periodic in the x and y directions. The background state of the carrier phase is established by accelerating the flow with an imposed pressure gradient, $-\mathrm{d}P/\mathrm{d}x > 0$ (note that $\hat{\boldsymbol{x}}$ is the unit vector in the streamwise direction) and allowing the flow to become turbulent. The magnitude of the pressure gradient allows us to define a friction velocity

Re_τ	Sv^+	St^+	g^+	St_η	Sv_η
315	0.025	10	2.5×10^{-3}	0.31–4.25	0.038–0.14
315	0.025	50	5×10^{-4}	1.58–21.25	0.038–0.14
315	0.25	10	2.5×10^{-2}	0.31–4.25	0.38–1.4
315	0.25	50	5×10^{-3}	1.58–21.25	0.38–1.4
315	0.8	10	8×10^{-2}	0.3–4.29	1.22–4.47
315	2.5	10	2.5×10^{-1}	0.31–4.25	3.8–14.0
315	2.5	50	5×10^{-2}	1.58–21.25	3.8–14.0
630	0.025	10	2.5×10^{-3}	0.24–4.7	0.037–0.16
630	0.025	50	5×10^{-4}	1.18–23.17	0.037–0.16
630	0.025	100	2.5×10^{-4}	2.38–46.33	0.037–0.16
630	0.25	10	2.5×10^{-2}	0.24–4.7	0.37–1.60
630	0.25	50	5×10^{-3}	1.18–23.17	0.37–1.60
630	0.25	100	2.5×10^{-3}	2.38–46.33	0.37–1.60
630	0.8	10	8×10^{-2}	0.24–4.7	1.17–5.21
630	2.5	10	2.5×10^{-1}	0.24–4.7	3.66–16.03
630	2.5	50	5×10^{-2}	1.18–23.17	3.66–16.03
630	2.5	100	2.5×10^{-2}	2.38–46.33	3.66–16.03
1260	0.8	10	8×10^{-2}	0.2357–6.29	1.0–5.21

Table 1. Table of cases discussed throughout the work. Parameter definitions can be found in the main text. The case with $Re_\tau = 1260$ was run on a 512^3 grid, all cases with $Re_\tau = 630$ were run on a 256^3 grid, while cases with $Re_\tau = 315$ were run on a 128^3 grid.

$u_\tau = \sqrt{\tau_w/\rho_a}$, where τ_w is the stress at the lower boundary. Using the friction velocity, the height of the domain, H, and viscosity of the carrier phase, we can define a friction Reynolds number of $Re_\tau = u_\tau H/\nu$. Friction Reynolds numbers for each simulation presented in this work can be found in table 1. This set-up is identical to that used in Grace *et al.* (2024).

We can define the local Kolmogorov time scale, velocity scale and acceleration scale,

$$\tau_\eta = \left(\frac{\nu}{\epsilon}\right)^{1/2}, \quad v_\eta = (\nu\epsilon)^{1/4}, \quad a_\eta = \left(\frac{\epsilon^3}{\nu}\right)^{1/4}, \tag{2.3}$$

respectively, which represent the smallest relevant length scales of the turbulence. These parameters will be used to characterize the turbulent flow below. In statistically stationary HIT, the above scales are constants, but for wall-bounded turbulence they depend on height. Since the turbulence intensity decreases with height outside of the very thin viscous sublayer adjacent to the wall, so too does the kinetic energy dissipation rate resulting in a height variation of the Kolmogorov microscales. When the TBL is horizontally homogeneous, the mean dissipation rate ϵ is a function of the distance from the solid boundary. Within the logarithmic layer, it scales as

$$\epsilon \sim O\left(\frac{u_\tau^3}{\kappa z}\right), \tag{2.4}$$

where u_τ is the friction velocity, and κ is the von Kármán constant. However, when calculating the Kolmogorov time scale, velocity scale and length scale, we use the dissipation computed in the DNS.

2.2. *Dispersed phase*

Our main focus is towards on-coarse dust transport in the atmospheric surface layer. Dust particles can range in size, but even coarse grains (roughly 30–100 μm) are significantly smaller than the local Kolmogorov scale, which can be in the range of several millimetres. Indeed, these particles are also significantly denser than the carrier phase, though their volume fractions can be quite low once they are above the emission layer. With these assumptions in mind, for each particle (the dispersed phase), we apply the point-particle approximation and apply the conservation of momentum for a rigid spherical particle subjected to linear hydrodynamic drag and gravity. Note that we have purposefully omitted particle lift as it has been shown to play negligible role in the dynamics discussed in the present work (Costa, Brandt & Picano 2020). Furthermore, as we are concerned with the dilute limit, two-way coupling and particle–particle interactions may be ignored. Since these particles are assumed to be much denser than the carrier phase, we may also ignore added mass and Basset history forces. The one-way coupled point particle approximation also has the added benefit that each particle is independent from each other particle, effectively removing the volume fraction as a governing parameter as the number of particles is increased. This allows us to increase the number of particles to ensure convergence of the statistics of interest without affecting the flow. As such, our results are assumed to be valid in the dilute limit, where particle densities are much greater than that of the fluid phase.

The equations of motion are

$$\frac{\mathrm{d}\boldsymbol{u}_p}{\mathrm{d}t} = \frac{\Psi}{\tau_p}(\boldsymbol{u}_f - \boldsymbol{u}_p) - \boldsymbol{g}, \tag{2.5}$$

$$\frac{\mathrm{d}\boldsymbol{x}_p}{\mathrm{d}t} = \boldsymbol{u}_p. \tag{2.6}$$

Here, $\boldsymbol{u}_p = (u_p, v_p, w_p)$ is the three-dimensional velocity vector for each particle, $\boldsymbol{x}_p = (x, y, z)$ is the location of each particle in space, $\boldsymbol{g}$ is the gravitational acceleration (which only affects accelerations in the z direction), $\boldsymbol{u}_f = (u_f, v_f, w_f)$ is the three-dimensional instantaneous flow velocity evaluated at the location of the particle. Much of our focus will be placed on the vertical component which we denote as w_f (not bold).

Particles are injected at the upper boundary at a random horizontal location with an initial velocity equal to the fluid velocity at their location. We have performed a sensitivity test to investigate the importance of the particle initial condition by comparing results when injected at their laminar Stokes settling velocity. We have concluded that the choice of initial particle velocities at injection makes a negligible quantitative change to our results, and does not affect the results qualitatively.

Particles are removed when they contact the bottom boundary, and once removed, are reinjected at a random horizontal location at the upper boundary. This maintains a constant particle number in the domain, and a constant vertical particle flux. Particles are allowed to come to statistical equilibrium, and statistics are recorded for no less than 100 eddy turnover times after this time. Finally, particles are allowed to rebound elastically off the upper boundary, and the particle boundary conditions are periodic in the horizontal directions.

The relaxation time scale of the particles, τ_p, is defined as

$$\tau_p = \frac{\rho_p d_p^2}{18\rho_a \nu}, \tag{2.7}$$

where ρ_p is the particle density, d_p is the particle diameter and the Stokes settling velocity is defined as $v_g = \tau_p g$. Here $\Psi = 1 + 0.15Re_p^{0.687}$ is the Schiller–Neumann correction to the drag force, and Re_p is the particle Reynolds number. The particle Reynolds number remains small enough such that $\Psi \approx 1$. For the theory discussed below in § 2.3, we follow Bragg *et al.* (2021*a*) and make the assumption that $\Psi = 1$ for analytical tractability.

We can now define a set of non-dimensional parameters characterizing the system,

$$St^+ = \frac{\tau_p u_\tau^2}{\nu}, \quad Sv^+ = \frac{v_g}{u_\tau}, \quad St_\eta = \frac{\tau_p}{\tau_\eta}, \quad Sv_\eta = \frac{v_g}{v_\eta}. \tag{2.8}$$

These are the friction Stokes number and the settling velocity parameter based on the viscous scales, and the Stokes number and the settling velocity parameter based on the local Kolmogorov scales. Here St_η and Sv_η are functions of the distance from the solid boundary, whereas St^+ and Sv^+ are constant parameters.

Other studies focused on particle settling define other parameters such as a Froude number, $Fr = a_\eta/g$, (Bec *et al.* 2014; Berk & Coletti 2021), or a scaled gravity

$$g^+ = \frac{g\nu}{u_\tau^3}, \tag{2.9}$$

which is simply the ratio of Sv^+ to St^+. These parameters are useful as they describe the relative role of gravitational accelerations and turbulent accelerations without referring to τ_p. We will refer to g^+ at various points throughout the discussion when necessary. The values for all parameters considered in this work, including the associated ranges of St_η and Sv_η, can be found in table 1.

2.3. *Statistics of inertial particles in a turbulent boundary layer*

We adopt the particle phase space approach used in Bragg *et al.* (2021*a*), focusing only on the vertical component of the particle equations of motion. First they define the particle probability density function (PDF) in position-velocity space as

$$\mathcal{P} = \langle \delta(z_p - z)\delta(w_p - w)\rangle, \tag{2.10}$$

which describes the distribution of the vertical components of the particle position and velocity, $z_p(t)$ and $w_p(t)$, in the phase space with coordinates z, w, and $\langle\cdot\rangle$ represents an ensemble average over all realizations of the system (note that δ represents the Dirac delta function). Note we make frequent use of conditional averages throughout this work, denoted by $\langle\cdot\rangle_{z,w}$ which is short hand for $\langle\cdot|z_p = z,\, w_p = w\rangle$. We can form an evolution equation for the PDF,

$$\frac{\partial \mathcal{P}}{\partial t} + \frac{\partial}{\partial z}\left(w\mathcal{P}\right) + \frac{\partial}{\partial w}\left(\langle a_p\rangle_{z,w}\mathcal{P}\right) = 0 \tag{2.11}$$

where we have defined $\langle a_p\rangle_{z,w} = \tau_p^{-1}(\langle w_f\rangle_{z,w} - w) - g$ as the vertical particle acceleration conditioned on $z_p = z$ and $w_p = w$ based on the vertical component of (2.5). The utility of this equation comes from the fact that we can derive evolution equations for each moment. Recall that the nth moment is defined as

$$\langle w_p^n\rangle_z = \frac{1}{\varrho}\int_{-\infty}^{\infty} w^n \mathcal{P}\,\mathrm{d}w, \tag{2.12}$$

where the notation $\langle\cdot\rangle_z$ represents an ensemble average conditioned on $z_p = z$ and ϱ is zeroth moment, which is related to the particle number concentration. Of importance to the present work will be the first and second moments (i.e. $n = 1$ and $n = 2$). The evolution

equation for the first moment is

$$\langle w_p \rangle_z = \langle w_f \rangle_z - v_g - \frac{\tau_p}{\varrho} \frac{\mathrm{d}}{\mathrm{d}z} \varrho \langle w_p^2 \rangle_z. \tag{2.13}$$

The details of the derivation of this equation can be found in Bragg *et al.* (2021*a*), and the general form of this equation (for the case where $v_g = 0$) for arbitrary moments can be found in Johnson *et al.* (2020). Equation (2.13) says that the average settling velocity comes from the average fluid velocity sampled by the particles, the laminar Stokes settling velocity, and a term that depends on the derivative of the mean square particle velocity which may be important near a solid boundary. For compactness, we can rearrange (2.13) into a relationship describing how the mean slip velocity varies with height,

$$\langle w_s \rangle_z = v_g + \frac{\tau_p}{\varrho} \frac{\mathrm{d}}{\mathrm{d}z} \varrho \langle w_p^2 \rangle_z, \tag{2.14}$$

where $\langle w_s \rangle_z = \langle w_f \rangle_z - \langle w_p \rangle_z$.

Our goal is to derive a continuum equation for the slip velocity variance. To do this, we multiply (2.11) by w^2 and integrate over all w. The full details of this operation can be found in Johnson *et al.* (2020). After integrating, we are left with the following relationship:

$$\frac{\mathrm{d}}{\mathrm{d}z} \varrho \langle w_p^3 \rangle_z - 2\varrho \langle a_p w_p \rangle_z = 0. \tag{2.15}$$

To expand the acceleration–velocity covariance, we expand to get $\langle a_p w_p \rangle_z = \langle w_f w_p \rangle_z - \langle w_p^2 \rangle_z$ and use the fact that $\langle w_s^2 \rangle_z = \langle w_f^2 \rangle_z - 2\langle w_f w_p \rangle_z + \langle w_p^2 \rangle_z$ to arrive at

$$2\langle a_p w_p \rangle_z = \frac{1}{\tau_p} (\langle w_f^2 \rangle_z - \langle w_s^2 \rangle_z - \langle w_p^2 \rangle_z) - 2\langle w_p \rangle_z g. \tag{2.16}$$

Putting (2.15) and (2.16) together, we get an equation for the mean squared slip velocity,

$$\langle w_s^2 \rangle_z = \langle w_f^2 \rangle_z - \langle w_p^2 \rangle_z - 2\langle w_p \rangle_z v_g - \frac{\tau_p}{\varrho} \frac{\mathrm{d}}{\mathrm{d}z} \varrho \langle w_p^3 \rangle_z. \tag{2.17}$$

Equation (2.17) indicates that the mean squared slip velocity variance is a function of the mean squared sampled velocity $\langle w_f^2 \rangle_z$, the mean squared particle velocity $\langle w_p^2 \rangle_z$, a drift due to the non-zero average vertical velocity $\langle w_p \rangle_z$ and the vertical derivative of the mean cubed particle velocity $\langle w_p^3 \rangle_z$, all of which are implicit functions of particle inertia and gravity.

At this point, an important distinction must be made. Though the above equation is valid for inertial particles settling through a TBL, it should be noted that when particles settle under gravity, the mean squared quantities are not equal to their variances in general. This arises from the non-zero average settling velocity. Thus, to derive a relationship between the variances, we must do a Reynolds decomposition of each term. The details of this process are omitted here, but can be found in Appendix A . The final relationship is

$$\langle {w_s'}^2 \rangle_z = \overbrace{\underbrace{\langle {w_f'}^2 \rangle_z - \langle {w_p'}^2 \rangle_z}_{(1)} + R_t}^{(2)} + R_g \tag{2.18}$$

where R_t and R_g are defined as

$$R_t = -\frac{\tau_p}{\varrho}\frac{\mathrm{d}}{\mathrm{d}z}\varrho\langle {w'_p}^3\rangle_z, \tag{2.19}$$

$$R_g = -\frac{\tau_p}{\varrho}\frac{\mathrm{d}}{\mathrm{d}z}\left(\varrho\langle w_p\rangle_z^3 + 3\varrho\langle w_p\rangle_z\langle {w'_p}^2\rangle_z\right) + 2\langle w_p\rangle_z(\langle w_s\rangle_z - v_g), \tag{2.20}$$

respectively. This model contains many terms and is quite complex, but it can be broken down into three parts, arranged in order of increasing problem complexity, and the level of complexity highlighted by the over and underbraces.

First, grouped under (1), are the terms that would appear for particles settling through homogeneous turbulence. In this limit, the slip velocity variance is determined exclusively by the difference between $\langle {w'_f}^2\rangle_z$ and $\langle {w'_p}^2\rangle_z$. This is the case for particles both with and without gravity, since gravity and inertia implicitly modify these terms. Next, grouped under (2), are the terms that appear for particles dispersing vertically through a TBL in the absence of gravity. Note that all terms encompassed by (1) are included in (2), but when considering those terms covered under (1) in the context of a TBL, they gain implicit height dependence since their magnitudes vary with the distance from the boundary. Furthermore, at this level, a new term appears, denoted by R_t. This term is proportional to the derivative of the product of the concentration and the particle velocity triple moment and increases with particle inertia. As $Sv^+ \to 0$, $\langle {w'_p}^2\rangle_z$ approaches $\langle w_p^2\rangle_z$, but R_t remains, regardless. Finally, by incorporating gravity, the mean particle velocity is no longer zero, leading to a new term grouped under (3), denoted by R_g. The quantities composing R_g are explicitly dependent on both the inhomogeneity of the flow through the vertical derivative, and the non-zero particle settling velocity. For clarity of interpretation, the second term on the right-hand side of (2.20) is written in terms of $\langle w_s\rangle_z - v_g$, which we can see from (2.14) is identical to $\tau_p/\varrho\mathrm{d}/\mathrm{d}z\varrho\langle w_p^2\rangle_z$. In summary, by considering the continuum equations for the first and second moment of the particle velocity, we have been able to derive an equation for the particle slip velocity. We have identified a hierarchy of terms that appear in homogeneous turbulence and TBLs with and without settling (grouped under (1)), those that appear in a TBL without settling (grouped under (2)) and those that appear in a TBL with settling (grouped under (3)). In the following section, we will identify the importance of these terms throughout the TBL.

3. Results

3.1. *Tendencies governing the slip velocity variance*

In this section, we consider vertical profiles of $\langle {w'_s}^2\rangle_z$, $\langle {w'_p}^2\rangle_z$, $\langle {w'_f}^2\rangle_z$ and R_g. Figure 2 shows the tendencies in (2.18) for several cases scaled by u_τ^2. For the results presented in this section, R_t was observed to be very small relative to the other terms in (2.18), and is omitted from figure 2. Note that all profiles of a given St^+ and Sv^+ in figure 2(*b*,*e*,*h*) and figure 2(*c*,*f*,*i*) when added together return the profiles shown in figure 2(*a*,*d*,*g*), as per (2.18). An example of this is shown in Appendix B . Each row corresponds to a different friction Stokes number highlighted on the left-hand side of the figure, while each curve on a given plot corresponds to a different value of Sv^+. Overall, this figure highlights the dominant tendencies controlling the slip velocity variance as St^+ and Sv^+ are independently changed.

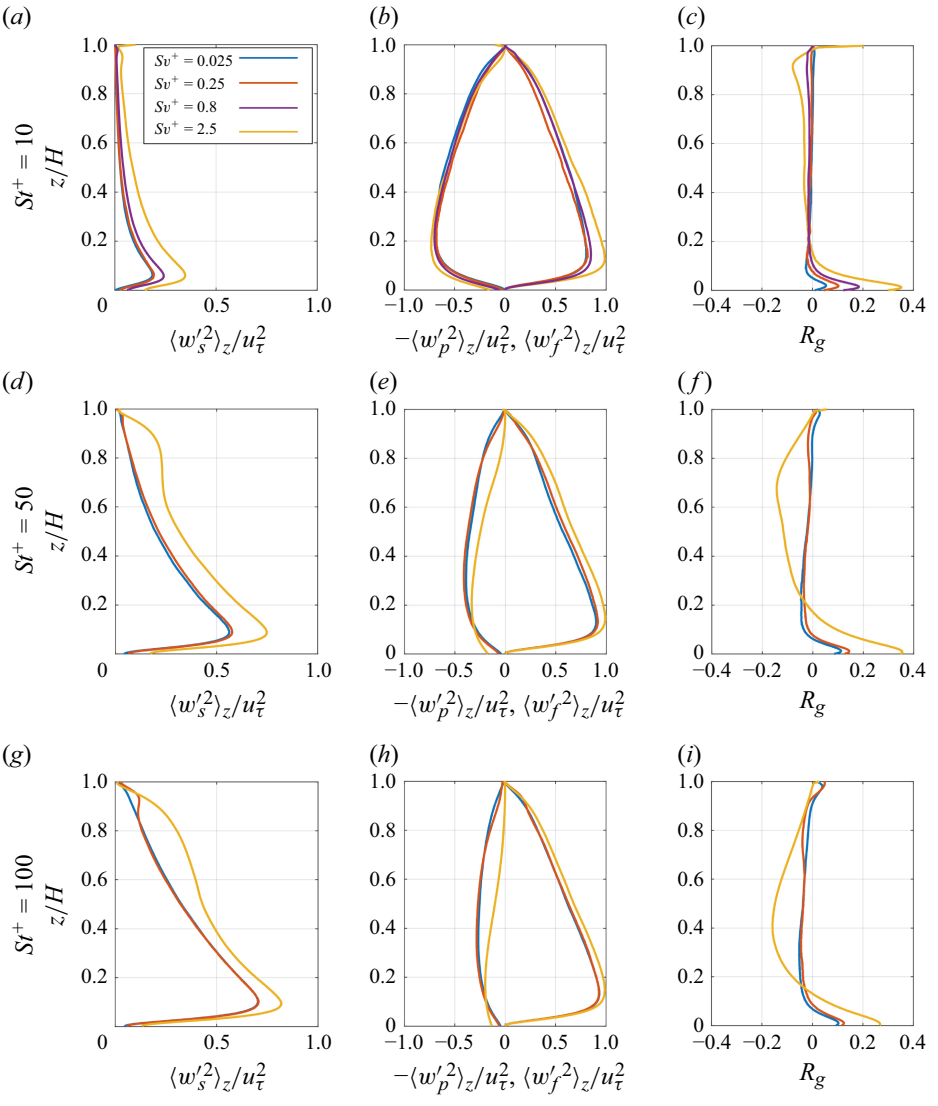

Figure 2. Controlling tendencies for the slip velocity variance according to (2.18) at $Re_\tau = 630$. Panels (*a*), (*d*) and (*g*) show the normalized slip velocity variance for each Sv^+, while (*a–c*), (*d–f*) and (*g–i*) are for a different value of St^+ (shown on the left-hand side of the figure). Panels (*b*), (*e*) and (*h*) show the (negative) velocity variance and the (positive) seen velocity variance. Panels (*c*), (*f*) and (*i*) show the contributions from R_g. Note that R_t is omitted from this figure as it is small across the entire domain relative to the other terms. All terms are normalized by u_τ^2.

Generally, the behaviour of the slip variance as a function of the vertical coordinate is qualitatively similar between all cases considered, evident from figure 2(*a*,*d*,*g*). However, the magnitude of the slip variance for a given case varies throughout the domain, and becomes increasingly sensitive to Sv^+ when Sv^+ approaches unity. This is evident in 2(*a*), where we see a negligible changes when Sv^+ is varied between 0.025 and 0.25, but larger changes as it is increased to 0.8 and beyond. For particles of $Sv^+ \sim O(1)$, we expect that the vertical turbulent velocities in the logarithmic region (which themselves scale in magnitude with u_τ) tend to be too weak on average to overcome the strong settling

velocity, and this leads to increasingly larger slip velocities. Within the logarithmic layer, the slip variance at constant Sv^+ (curves of fixed colour) tends to increase rapidly between $St^+ = 10$ and $St^+ = 50$, but more slowly between $St^+ = 50$ and $St^+ = 100$. This occurs because the particle velocity variance rapidly decreases in magnitude towards zero, while the variance of the fluid velocity seen by the particle does not, evident by considering figure 2(*b*,*e*,*h*). However, very near the solid boundary (i.e. below $z/H = 0.1$), the variance of the fluid velocity seen by the particle approaches zero, while the particle velocity variance remains finite. This is also where R_g is relatively large, indicating that the primary terms that control the slip variance very near the wall are these terms and negative particle velocity variance.

Likewise, the slip variance at constant St^+ tends to increase most rapidly as Sv^+ surpasses unity. This is due to the fact that particles tend to settle out of locally correlated regions of turbulence faster than they would in the absence of settling, thus experiencing a higher variance in accelerations, and thus their slip velocity. Interestingly, there is some variation in the variance of the fluid velocity seen by the particle with Sv^+. This dependence arises due to the preferential sampling of the fluid velocity field, and the mechanisms responsible for this are essentially the same as those responsible for $\langle w_f \rangle_z$ deviating from zero for an inertial particle (see detailed discussion in Bragg *et al.* (2021*a*)).

Lastly, R_g, shown in figure 2(*c*,*f*,*i*), are non-zero but are not leading order within the interior of the domain (note the change in the scale of the horizontal axes of these panels), though they are relatively important within the viscous sublayer. Note that above $z/H = 0.1$, these terms are almost completely negligible aside from when $Sv^+ = 2.5$. It is important to note that previous studies (Gerashchenko *et al.* 2008; Lavezzo *et al.* 2010) have shown that the impact of fluid shear and wall-normal gravity on inertial particle accelerations is most pronounced in the buffer layer $z^+ < 50$. When normalized against the large-scale parameters of the flow (at $Re_\tau = 630$), this height corresponds to a height of roughly $z/H < 0.1$, so it should be expected that it is R_g that strongly influences the slip velocity variance in that region of the flow.

In summary, these profiles highlight the fact that within the logarithmic layer, the slip variance is primarily governed by the differences between the variance of the flow velocities sampled by the particles and the particle velocity variance, with contributions coming from R_g when Sv^+ increases beyond unity. However, it is clear that higher-order moments of the continuum equations (encoded in R_g) may be subleading and negligible in most other cases. It is not until the viscous sublayer where the contribution from R_g becomes significant in determining the slip variance. Furthermore, the subleading behaviour of R_g in the logarithmic layer does not imply that the inhomogeneity of the turbulence is irrelevant. In fact, the remaining terms ($\langle {w'_f}^2 \rangle_z$ and $\langle {w'_p}^2 \rangle_z$) may have implicit dependence on the inhomogeneity of the turbulence, and this will be discussed later.

As the particles settle, they experience a mean vertical slip velocity according to (2.14), and they also experience a mean horizontal slip due to both the mean shear and the height dependent correlations between horizontal and vertical particle velocity fluctuations. Figure 3 illustrates the relative contribution of the slip fluctuations to the overall slip velocity by considering two metrics: the integrated relative slip, and the integrated slip variance. These metrics are defined as

$$\varphi_r^{(i)} = \frac{1}{D}\int_D \frac{\langle {u'_{s,i}}^2 \rangle_z}{\langle u_{s,i} \rangle_z^2 + \langle {u'_{s,i}}^2 \rangle_z} \mathrm{d}z, \quad \varphi_s^{(i)} = \frac{1}{D}\int_D \frac{\langle {u'_{s,i}}^2 \rangle_z}{u_\tau^2} \mathrm{d}z, \tag{3.1}$$

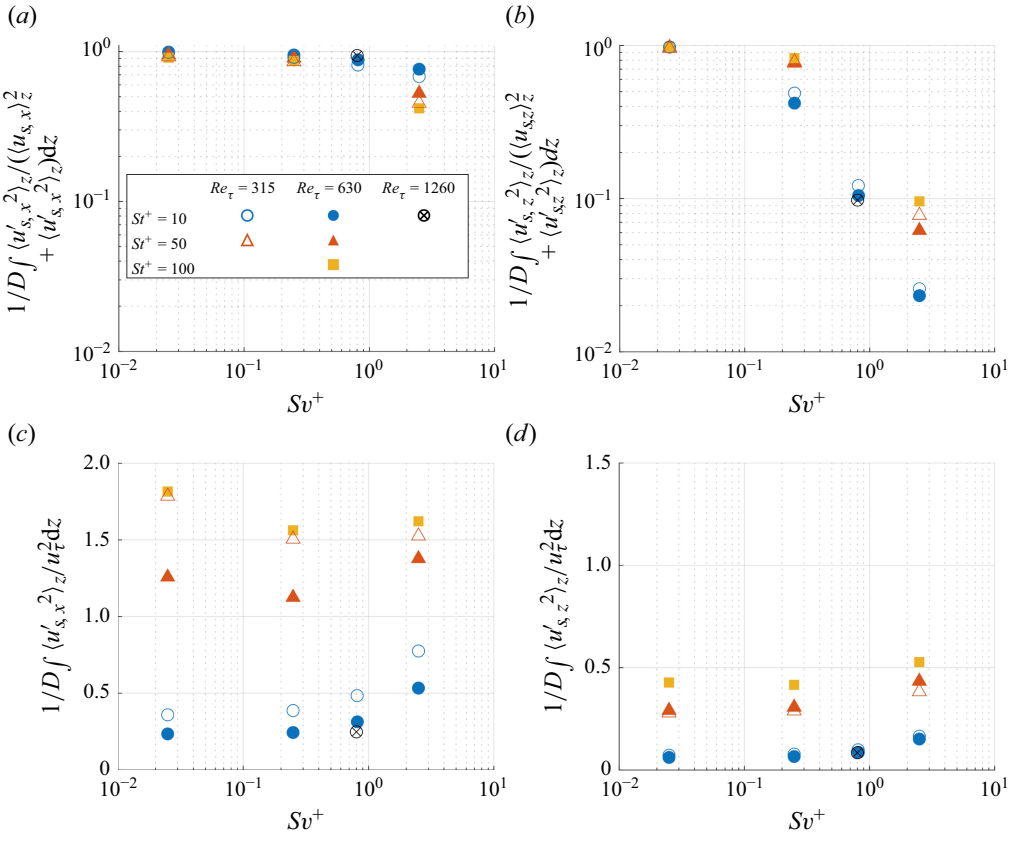

Figure 3. The horizontal and vertical components of $\varphi_r^{(i)}$ (panels (*a*) and (*b*)) and $\varphi_s^{(i)}$ (panels (*c*) and (*d*)) for all cases in table 1 plotted against Sv^+. The filled markers correspond to cases at $Re_\tau = 630$, while the open-faced markers correspond to cases at $Re_\tau = 315$.

respectively, where D is the vertical subregion of the domain between $z^+ = 50$ and $z/H = 0.75$ and $i = x,\ z$ (we have temporarily adopted this notation for compactness). We have chosen this subregion as it represents the logarithmic region of the flow – these bounds were chosen to eliminate edge effects from the upper boundary condition, and our results are not qualitatively affected by the choice of the bounds of integration. The integrated relative slip helps us to understand the relative importance of the slip fluctuations relative to the mean slip, while the integrated variance provides a simple metric to assess the average slip variance. The integrated relative slip is shown for the horizontal (streamwise) and vertical components of the slip variance (there is no mean slip in the spanwise, so this component is ignored for this discussion) in figures 3(*a*) and 3(*b*), while the components of the integrated slip variance are shown in figures 3(*c*) and 3(*d*). Each marker style corresponds to a different value for St^+, and the results are plotted against Sv^+ to highlight the role of settling. Filled markers correspond to runs with $Re_\tau = 630$, empty markers correspond to runs with $Re_\tau = 315$, and the empty marker filled with a cross corresponds to the run with $Re_\tau = 1260$. Note that since this is an integrated quantity, there is necessarily no information regarding the vertical structure of the profiles. However, an analysis of the profiles themselves (not shown) would provide the same conclusions.

Figure 3 shows that fluctuations of the slip velocity are less important at larger values of Sv^+. For example, for small Sv^+ (independent of St^+), the normalized variance is nearly unity, indicating that the slip variance induced by the turbulent fluctuations are the leading-order controller of the overall slip velocity for both the horizontal and vertical components. However, we can see that by increasing Sv^+, there is a decrease in the relative slip variance for both components. The reason for this is clear from an examination of figures 3(*c*) and 3(*d*), which show the integrated slip variance in the horizontal and the vertical, respectively. We can see that in a bulk sense, the slip variance in both directions does not strongly vary with Sv^+ (except for perhaps particles with $St^+ = 10$ in the horizontal). The implication is that the strong decrease in the relative variance in figure 3(*b*) (the vertical component) does not come from a decrease in the magnitude of the slip variance itself, but instead a strong increase in the magnitude of the mean slip induced by gravitational settling. Moreover, the same mechanism does not occur in the horizontal slip variance, as the decrease in the normalized slip variance is not nearly as strong. Furthermore, as Sv^+ increases, particles with $St^+ = 10$ have the largest change in the vertical relative slip variance due to their small slip variance values. This is indicative of the fact that these particles most faithfully follow the flow in the absence of gravity, and as a result, are most sensitive to the growing mean slip as Sv^+ increases.

We also briefly consider a comparison between several Reynolds numbers. There are some slight differences in these metrics as the Reynolds number is varied between 315 and 1260. Here, changes in the relative slip variance are more strongly reflected in the vertical component. As the Reynolds number is increased, the relative slip variance in the vertical, figure 3(*b*), decreases. Since there are only small variations in the integrated slip variance as the Reynolds number is increased, the change in the integrated relative variance come from changes in the mean slip. The explanation for this change is as follows. Appearing in the equation of the mean slip, (2.14), is the term $\tau_p/\varrho(\mathrm{d}/\mathrm{d}z)\varrho\langle w_p^2\rangle_z$, which represents the combined effects of turbophoresis and diffusion-like behaviour near the solid boundary. It is known from Bragg *et al.* (2021*a*) that this term is negative within the logarithmic region of the flow, representing a mechanism that decreases the slip velocity. However, this term tends to be significant only near the solid boundary for a given τ_p, so as the Reynolds number increases, the relevance of this term is diminished when integrated across the region D. Therefore, in the integrated sense, $\langle w_s\rangle_z^2$ tends to increase towards v_g^2 when Re_τ increases which results in a decrease in $\varphi_r^{(3)}$. However, this conclusion is only qualitative as more data at higher Reynolds numbers are necessary to make more quantitative conclusions.

The conclusion of figure 3 is that while the overall slip magnitude in the horizontal may be controlled by the slip fluctuations, the mean may end up being the main controller of the slip in the vertical at large Sv^+ and small to moderate St^+, but the relative importance of the mean may be impacted by the Reynolds number of the flow.

3.2. *Relationship to the acceleration statistics*

The slip velocity statistics are directly related to the acceleration statistics of the particles. By considering the acceleration statistics, we can gain an understanding of how strongly gravity implicitly modifies the drag felt by the particles as they traverse the TBL. Moreover, the acceleration variance often gives a clue regarding the turbulent structures which particles are interacting with. For example, Yeo, Kim & Lee (2010) showed that the elongated tails of fluid particle acceleration PDFs within the buffer layer and viscous sublayer are due to the vortical structures impinging on the viscous sublayer. Lavezzo *et al.* (2010) attributed changes in the vertical and streamwise acceleration variance of settling

inertial to these same vortical structures. In a two-way coupled turbulent Couette flow, Richter & Sullivan (2013) found that particles tend to damp vertical fluctuations of the near wall dynamics, suggesting a complex feedback cycle.

In the limit of $g^+ \to 0$ (recall that $g^+ = Sv^+/St^+$), or when gravitational accelerations are ignored *a priori*, Bec *et al.* (2006) demonstrated that particles tend to cluster in strain dominated regions of the flow for low Stokes number (i.e. $St_\eta \lesssim 0.3$), leading to a decrease in the acceleration variance of the particles. At larger Stokes number, the acceleration variance continues to decrease, but is instead due to inertial filtering; particles can no longer respond to turbulent fluctuations with time scales greater than τ_p^{-1}. Ultimately, both processes work to reduce the acceleration variance, but for different reasons (Bragg, Ireland & Collins 2015). However, by introducing gravity, particles can settle out of strain-dominated regions of the flow, which may actually contribute to an increase in their acceleration variance, and this often referred to as the crossing trajectory mechanism (Csanady 1963). Ireland *et al.* (2016) and Berk & Coletti (2021*a*) showed that the importance of the crossing trajectories mechanism on the acceleration statistics is due to both St_η and Sv_η (or alternatively $1/Fr = g/a_\eta$). They showed that for large g/a_η (equivalent to large g^+ in our context), gravitational accelerations become increasingly important to the dynamics, leading to a peak in the acceleration variance at sufficiently high g/a_η, around $St_\eta = O(1)$. In the following results, we highlight some similarities of the computed slip and acceleration variance to results from Berk & Coletti (2021), who focused on modelling the slip and acceleration variance in homogeneous turbulence in terms of the variance of the fluid along the particle trajectory. Our goal is to compare our model results in a TBL with the predictions of their model for homogeneous turbulence (derived in Appendix C).

First, we consider profiles of the relative slip variance, which we define as $\langle {w_s'}^2 \rangle_z / \langle {w_f'}^2 \rangle_z$, shown in figure 4(*a*). Here we again focus on the region D, which is the region between $z^+ = 50$ and $z/H = 0.75$, in order to omit effects from viscous sublayer and the upper boundary condition, respectively (denoted by black dashed lines on the figure). The general trend is that by increasing Sv^+ at a given St^+, the relative slip variance tends to increase, with the most dramatic increase coming as Sv^+ is increased beyond unity, which is probably a reflection of the crossing trajectories mechanism. Furthermore, we can see that relative change between $Sv^+ = 0.25$ and $Sv^+ = 2.5$ decreases as St^+ increases. The reason for this is discussed more below.

We can also consider the relative acceleration variance, $\langle {a_p'}^2 \rangle_z / \langle {w_f'}^2 \rangle_z \tau_\eta^{-2}$, plotted against the local value of St_η, shown in figure 4(*b*). We can see that as the range of St_η increases (by changing St^+), the relative acceleration variance approaches the asymptotic relationship St_η^{-2}, i.e. is a decreasing function of the particle stokes number. So, in spite of the slip variance increasing with particle inertia at fixed Sv^+ (evident in figure 4*a*), it does so at a slower rate than St_η^2, meaning that the particle acceleration variance decreases with particle inertia. This agrees with the work of Lavezzo *et al.* (2010), who showed that the vertical particle acceleration variance decreased as St^+ was increased at fixed Sv^+. Note that in their study, they considered a fixed $g^+ = Sv^+/St^+$, but the conclusions presented here are the same. However, for moderately inertial particles, characterized by the $St^+ = 10$ cases, there is more potential for gravity to increase the relative acceleration variance. For example, due to the crossing trajectories mechanism, we can see that when $Sv^+ = 2.5$ for these particles, the acceleration variance is much larger, and tends to scale as St_η^{-1}, which is consistent with the results from Balachandar (2009) when $\tau_\eta \ll \tau_p \ll \tau_{l,p}$ and from Berk & Coletti (2021) in roughly the same range of St_η. From figure 4(*b*), we can see that the crossing trajectories mechanism is not strong for large

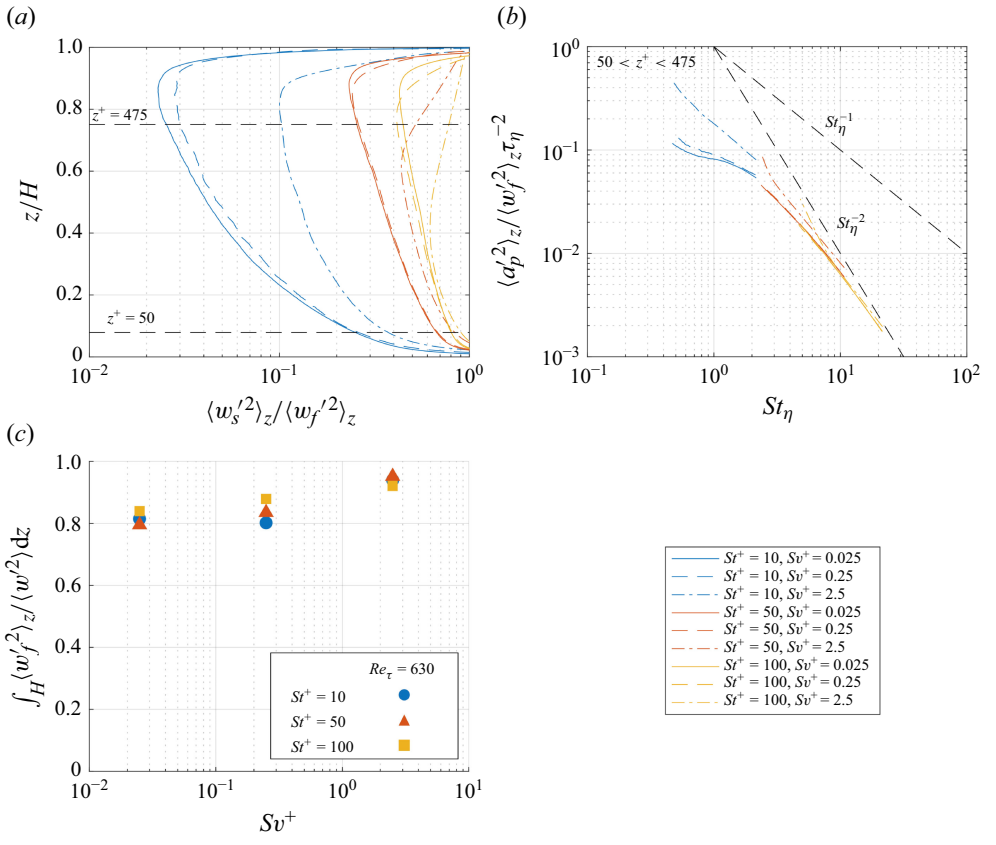

Figure 4. Panel (*a*) shows the slip variance normalized by the seen variance for all cases in table 1 at $Re_\tau = 630$. The horizontal dashed lines denote heights of $z^+ = 50$ and $z/H = 0.75$. Panel (*b*) shows the normalized acceleration variance over the same range plotted against the local value of St_η, while the dashed line represents the St_η^{-2} scaling. The colours of each curve in panels (*a*) and (*b*) correspond to values of St^+, while the line styles correspond to values of Sv^+. Panel (*c*) shows ratio of the seen variance to the unconditional variance averaged over the entire vertical extent plotted against Sv^+ for all cases at $Re_\tau = 630$.

St^+ particles, since these particles approach the asymptotic St_η^{-2} scaling across the entire TBL. The implication here is that extremely inertial particles tend not to respond to high frequency and intermittent turbulent fluctuations associated with changes in the sampled fluid environment anywhere across the TBL. However, when particles are moderately sized, such that they achieve $St_\eta \sim 1$ there is a region within the logarithmic layer of the TBL where they become susceptible to crossing trajectory effects, and this leads to an increase in their relative acceleration variance.

As a final point on this discussion, a potential shortcoming of analysing the relative slip variance and the relative acceleration variance is that they are written in terms of the fluid velocity variance along the particle trajectory, which is an unknown quantity *a priori*. We can relate this to the unconditional variance, for which there are well-known models (see Kunkel & Marusic (2006) for example). In figure 4(*c*) we show the vertically integrated ratio of the vertical components of the fluid velocity variance along particle trajectories to the unconditional fluid velocity variance against Sv^+. This integrated ratio approaches unity as Sv^+ increases implying that the seen variance approaches the unconditional variance in this limit. Moreover, this ratio is no less than roughly 0.8 for our range of

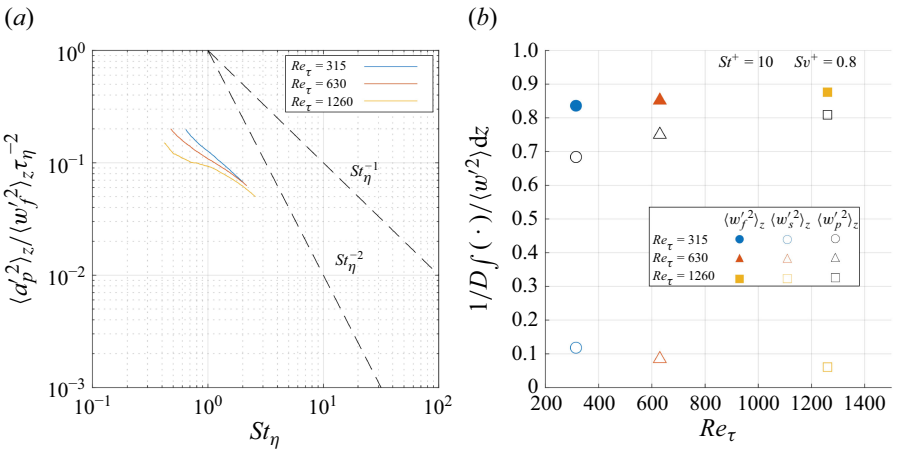

Figure 5. Panel (*a*) shows the normalized acceleration variance for cases with $St^+ = 10$ and $Sv^+ = 0.8$ at three different Reynolds numbers as a function of St_η. Panel (*b*) shows the seen variance (filled markers), slip variance (coloured empty markers) and particle velocity variance (black markers) normalized by the unconditional variance integrated over the range D as a function of Re_τ.

parameters, implying an acceptable correspondence between these two quantities. This is significant for modelling purposes as our results show that the fluid velocity variance along the particle trajectory may be substituted for the seen variance in a TBL without incurring significant error, having implications for the predictive power the particle statistics in a TBL. Berk & Coletti (2021) also arrived at this conclusion in homogeneous turbulence.

We can also consider the impact of Reynolds number on the relative acceleration variance, as well as the averaged components of (2.18). We can see in figure 5(*a*) the relative variance decreases as a function of St_η, as we would expect based on figure 4, but it is interesting that increasing Re_τ further decreases the relative acceleration variance. The reason for this is shown in figure 5(*b*). Both the the averaged fluid velocity variance seen by the particles (filled markers), and the particle velocity variance (empty markers; black outline) increase with Re_τ, but since the particle velocity variance increases faster with Re_τ, the net effect is a decrease in the slip variance with increasing Reynolds number (and consequently the relative acceleration variance since they are related through τ_p). The increases in $\langle {w'_f}^2\rangle_z$ and $\langle {w'_p}^2\rangle_z$ with Reynolds number when averaged across the domain is probably due to the increasing size of the quasihomogeneous region of the flow (Kunkel & Marusic 2006). Models of the unconditional vertical fluid velocity variance suggest that this quantity asymptotically approaches a constant in the limit of high Reynolds number. Though our Reynolds numbers are still quite low with regards to those found in the atmospheric surface layer, this notion can still provide some guidance to interpreting our data. As both $\langle {w'_f}^2\rangle_z$ and $\langle {w'_p}^2\rangle_z$ are related to the unconditional fluid velocity variance in some way, we expect that they should follow this behaviour, at least qualitatively. Finally, R_g and R_t are non-zero within the interior of the domain, but their magnitude, discussed later, is secondary to both $\langle {w'_f}^2\rangle_z$ and $\langle {w'_p}^2\rangle_z$ when taking the average across the logarithmic layer (recall the D does not include the viscous sublayer).

To conclude this section, we comment on the applicability of the model proposed by Berk & Coletti (2021) for $\langle {w'_s}^2\rangle_z$ (which we will refer to as BC2021 within the text). A sketch of the derivation of their model is presented in Appendix C . In short, they invoke an argument from Csanady (1963) to relate the particle velocity variance to the seen fluid

energy spectrum. They then use the fact that the fluid energy spectrum along the particle trajectory is the Fourier transform of the autocorrelation of the fluid velocity along the particle trajectory, which they represent using a two time scale model derived by Sawford (1991). The autocorrelation function involves the decorrelation time scale of the turbulence along the particle trajectory, $\tau_{l,p}$, for which they use the model derived in Csanady (1963). This model assumes that the turbulence is homogeneous and isotropic, and thus particles experience no spatial change in the statistics of the turbulence along their trajectory. Our goal is to compare how the computed relative slip variance within the TBL compares with the modelled slip variance in BC2021. As BC2021 was developed under the assumption of homogeneous turbulence, we can extend it to a TBL by making a locally homogeneous approximation, meaning that any change the slip variance with height is occurs due to local changes in the turbulent dissipation. For brevity, we will refer to the slip variance modelled by BC2021 as BC. We first consider (2.18) normalized by the seen variance,

$$\frac{\langle {w_s'}^2\rangle_z}{\langle {w_f'}^2\rangle_z} = \overbrace{\underbrace{1 - \frac{\langle {w_p'}^2\rangle_z}{\langle {w_f'}^2\rangle_z}}_{PV} + \frac{R_t}{\langle {w_f'}^2\rangle_z} + \frac{R_g}{\langle {w_f'}^2\rangle_z}}^{M}. \tag{3.2}$$

We have highlighted two subsets of these terms. First, we denote the first two terms on the right-hand side of (3.2) as PV (for 'particle velocity'). Our focus on this subset of terms is motivated by the BC2021 model (derived in Appendix C). The model BC2021 was developed for settling particles in homogeneous turbulence, meaning that there are no spatial variations in the turbulent statistics. This implies that R_g and R_t play no role in the dynamics, which leaves behind only the $\langle {w_f'}^2\rangle_z$ and $\langle {w_p'}^2\rangle_z$ terms. We also denote the full right-hand side of (3.2) as M (for 'model'). As we have discussed previously, our analysis will be limited to the logarithmic region of the flow. We also comment (but do not show) that the variance predicted by BC2021 is smaller in magnitude than the slip variance computed by the DNS throughout this region.

First, we consider how BC2021 compares with the full right-hand side of (3.2), (denoted by M) which includes R_t and R_g (recall that R_t and R_g cannot appear in BC2021 *a priori* due to their assumption of homogeneous turbulence). Specifically, we consider the metric

$$\xi_1 = \frac{1}{D}\int_D \|M - BC\|\mathrm{d}z, \tag{3.3}$$

which is plotted in figure 6(*a*). Here, ξ_1 represents the difference between the DNS data (which includes R_t and R_g) and the BC2021 model averaged over the region D. The main point here is that the differences between the BC2021 and M are relatively small. This should be the case since the buffer layer and viscous sublayer where R_t and R_g are expected to be most important has been omitted in D.

This motivates our second comparison between PV and the BC2021 model (BC); mathematically, we consider

$$\xi_2 = \frac{1}{D}\int_D \|PV - BC\|\mathrm{d}z, \tag{3.4}$$

which is shown in figure 6(*b*). Here, ξ_1 represents the difference between the DNS data omitting R_t and R_g and the BC2021 model averaged over the region D. This metric highlights a disparity between the DNS data and BC2021, but the differences amount to no

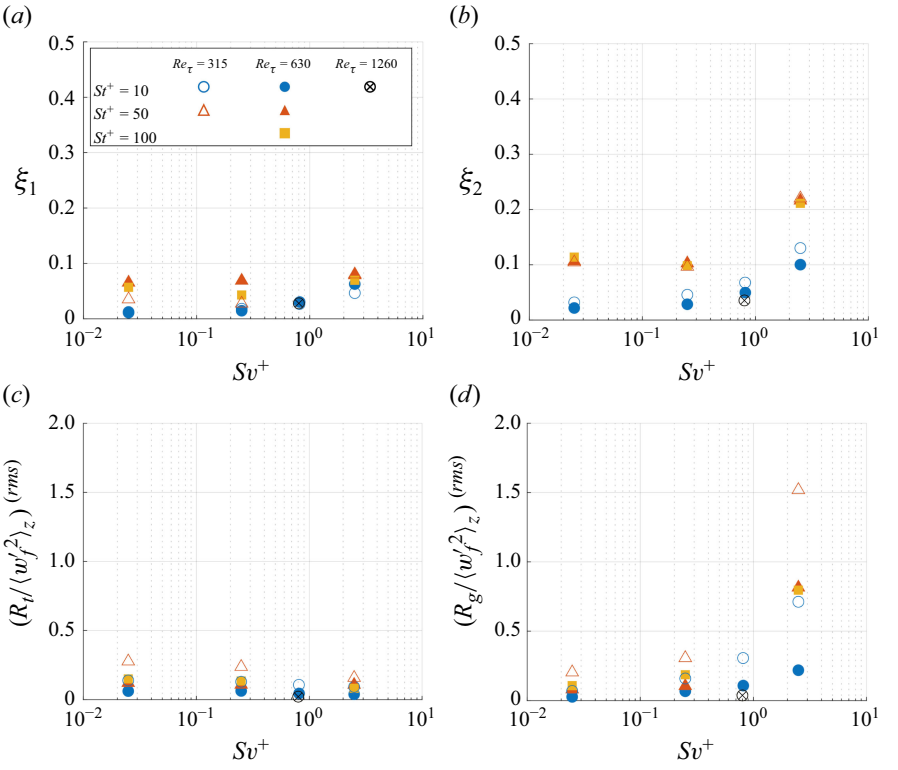

Figure 6. Shown in panels (*a*)–(*d*) are ξ_1, ξ_2 and the root mean squares (r.m.s.) values of R_t and R_g normalized by the seen variance for all cases in table 1, respectively. Open-faced markers represent cases with $Re_\tau = 315$, filled markers represent cases with $Re_\tau = 630$ and the marker with an $\otimes$ symbol represent the case with $Re_\tau = 1260$.

more than roughly 0.3. This discrepancy may come from several sources; one may be due to the fact that the underlying statistics of the turbulent flow change along the particle's trajectory due to the presence of the wall. This behaviour is reflected in the general increase of ξ_2 as Sv^+ increases, and will be discussed more in § 4. It is also interesting to note that there are differences associated with St^+, and these differences tend to plateau at large St^+ for fixed Sv^+.

Interestingly, from figures 6(*a*) and 6(*b*), it appears that the inclusion of R_t and R_g (which did not occur in BC2021) actually work to decrease the associated differences between the DNS and BC2021. However, as we established figure 2(*c*,*f*,*i*), R_g is primarily negative, causing a reduction of the relative slip variance. As we noted previously, M underestimates the computed relative slip variance within the logarithmic region of the turbulence, and the result is a decrease in the differences between the BC2021 and the DNS data. Moreover, by considering the r.m.s. of R_t and R_g normalized by $\langle w_f'^2\rangle_z$, shown in figures 6(*c*) and 6(*d*), we can see that R_g more important tendency, rather than R_t. Again, the importance of this term appears when both St^+ and Sv^+ are large, but decreases significantly as Re_τ increases.

Moreover, there are likely to be differences between the DNS data and BC2021 associated with the relatively small Reynolds numbers considered in this study. Within BC2021, there are several semiempirical models required to calculate characteristic parameters (i.e. C_0 and a_0; see Appendix C) of the turbulence, and there may be

an associated error incurred when the Reynolds number is low (for example, see the discussion in Lien & D'Asaro (2002)). However, we can see that by increasing Re_τ, the differences between the DNS and BC2021 tend to decrease suggesting a correspondence at large enough Reynolds number.

In summary, BC2021 gives a reasonable estimate for the DNS data in the logarithmic region of the flow. However, at large St^+ and Sv^+, the size of the differences increases, and this is due to combination of the changing statistics of the turbulence along the particle trajectories, as well as the low Reynolds numbers in the DNS, and how these are represented within BC2021. However, an important conclusion is that at large Reynolds number, we expect correspondence between the DNS data and BC2021, evidenced by the fact that the differences between BC2021 and the DNS decrease in this limit. Moreover, outside of the viscous sublayer, the importance of R_t and R_g will also be reduced as Re_τ increases, meaning correspondence between predictions by the BC2021 model and the variance measured in a TBL will become stronger in this limit. These results suggest that when St^+ and Sv^+ are not too large, we can estimate the slip variance in the logarithmic region of the flow by using BC2021 without incurring significant error.

4. Summary and discussion

4.1. *Summary*

Motivated by coarse particle transport in the atmospheric surface layer, we used coupled Eulerian–Lagrangian simulations to simulate the dynamics of ensembles of inertial particles in boundary layer turbulence. We examined the impact of particle inertia and settling on the mean and fluctuating particle slip velocity. We adapted a mathematical model discussed in Bragg *et al.* (2021*a*) and Johnson *et al.* (2020) for the slip velocity variance for settling inertial particles in a TBL and highlighted the controlling factors throughout the domain. We showed that to leading order, the slip variance above of the viscous sublayer was determined by the difference between the seen variance, $\langle {w'_f}^2 \rangle_z$, and the particle velocity variance $\langle {w'_p}^2 \rangle_z$, except for the largest value of Sv^+, where all terms in (2.18) became comparable. Consequently, as changes in the seen variance were relatively small, changes in the slip variance within the logarithmic layer were primarily governed by a decrease of the particle velocity variance, which was implicitly a function of particle inertia and the particle settling velocity (more on this below). Within the viscous sublayer, the balance became more complicated. In all cases, $\langle {w'_f}^2 \rangle_z$ tended towards zero to adhere to the no-slip condition enforced at the bottom boundary. However, the slip variance remained finite as the particles tended towards $z^+ = 0$ as $\langle {w'_p}^2 \rangle_z$, R_t and R_g remained finite. The higher-order terms tended to peak within this layer, and the magnitude of the peak tended to increase with Sv^+. However, by using domain averages, we demonstrated that the relative magnitude of the higher-moment terms tended to decrease as the Reynolds number increased, reflecting the fact that at higher Reynolds number, the viscous sublayer becomes much thinner, leading to a smaller contribution when averaged across the domain. As discussed above, these terms may still be important within the viscous sublayer depending on particle parameters, though.

We also showed that the fluid velocity variance along the particle trajectories exhibited only small changes with St^+, Sv^+ and Re_τ, and was approximately 80 % of the unconditional fluid velocity variance when averaged across the domain. The differences between the seen and unconditional variances are largest at the smallest Sv^+ considered

in this work, though the differences are still relatively small. These differences are likely a result of the relatively large spectrum of turbulent motions at high Reynolds number, and the impact of crossing trajectories, which works to implicitly affect the seen variance (see the discussion in Csanady (1963), for example). This conclusion is quantitatively consistent to the conclusions presented in Berk & Coletti (2021) for their laboratory experiments in homogeneous turbulence. This correspondence is significant as the seen variance is not known *a priori*. There exist approaches to modelling this quantity (Pozorski & Minier 1998; Minier & Peirano 2001), but the results of our work suggest that even in a TBL where there is spatial dependence in the variance of the turbulent quantities, we can approximate the fluid variance along the particle trajectories with the unconditional fluid variance without introducing significant errors. While this reduces the overall accuracy of the slip variance estimate, it increases the predictive power at the field scale, as models for the unconditional variance, such as those discussed in Kunkel & Marusic (2006), can be employed.

To examine the relative importance of the fluctuating and mean slip, we considered the ratio of the slip variance to the total mean squared slip velocity, $\langle {w_s}^2 \rangle_z$ (i.e. the square of the mean plus the fluctuation). We found that relative to the mean, the vertical slip variance decreased much faster than the horizontal as Sv^+ was varied. However, for both components, we showed that the overall magnitudes in the average sense did not change significantly, indicating that at relatively large Sv^+, the mean slip was the determining factor in the vertical, while the fluctuating slip was the determining factor in the horizontal. This effect was also accentuated for the smallest particles considered, due to their relatively small slip variance. To further complicate the behaviour, the relative size of the slip variance tended to decrease as the Reynolds number was increased, though due to computational restrictions, we can only provide limited guidance on this issue.

We also compared the slip variance computed by the DNS with a model derived for HIT by Berk & Coletti (2021) (as no such model currently exists for a TBL and is the focus of future work). The main conclusion is that the globally averaged differences (in the absolute sense) were relatively small, but the higher moment terms act as a confounding factor to reduce differences between the model and the DNS data. Thus, care should be taken when extrapolating results from low Reynolds number DNS in TBLs to higher Reynolds number experiments in homogeneous turbulence. However, as we know the size of higher moment terms tends to decrease as Reynolds number increase when integrated across the domain, we expect that DNS at higher Reynolds number should tend towards the results derived in Berk & Coletti (2021) outside of the thin viscous sublayer.

Additionally, due to the inhomogeneous nature of the turbulence, non-local effects implicit to $\langle {w'_f}^2 \rangle_z$ and $\langle {w'_p}^2 \rangle_z$ may occur at large Sv^+ and St^+. Isolating the importance of non-local effects in a TBL is the focus on ongoing research (for a recent example for a model of $\langle {w'_p}^2 \rangle_z$ in a TBL, see Zhang, Bragg & Wang (2023) and references therein), but incorporating them in a model is beyond the scope of the current article. These effects may arise due to the fact that the statistics of the turbulence may change significantly as the particle travels vertically. For example, consider the distance a settling particle travels over one relaxation time: $\delta \sim |\tau_p \langle w_p \rangle_z|$, where $\langle w_p \rangle_z$ is the average particle settling velocity conditioned on a height z given by (2.13). In order for the particle trajectory to be altered, turbulent fluctuations must be correlated over this distance. However, if this distance is comparable to the distance over which the characteristics of the turbulence change, then we expect that the particle feels the inhomogeneous nature of the flow. To formalize this quantitatively, consider the local turbulent kinetic energy at a height z, k. Taylor expanding

about this point and truncating after the second term, we have

$$k(z-\delta) = k(z) - \delta \left.\frac{\mathrm{d}k}{\mathrm{d}z}\right|_z . \tag{4.1}$$

To make a locally homogeneous approximation about the turbulence, we must have that

$$k(z) \gg \delta \left.\frac{\mathrm{d}k}{\mathrm{d}z}\right|_z , \tag{4.2}$$

i.e. the kinetic energy in a small neighbourhood about z (defined by the distance δ) is primarily defined by the kinetic energy measured at a height z. Using (4.1), we can estimate under what conditions a locally homogeneous approximation would be appropriate by looking for cases where the second term is small compared with the first. By assuming that the gradient of the turbulent kinetic energy scales as $u_\tau^2 z^{-1}$ (also implying k can be scaled by u_τ^2) (Smits *et al.* 2011) we have that $z \gg \delta$. By normalizing both sides of this inequality by the r.m.s. turbulent velocity, $u' = k^{1/2}$, we can write δ in terms of the sum of the settling enhancement, $E = (\langle w_p \rangle_z + v_g)/u'$ and v_g, (Good *et al.* 2014; Loth 2023) as

$$\tau_p \left| E + \frac{v_g}{w'} \right| \ll \frac{z}{u'}. \tag{4.3}$$

Now normalizing by τ_η, and observing that $u' \sim u_\tau$, we can simplify both side of this inequality to reveal that

$$St_\eta \, |E + Sv_\ell| \ll \left(\frac{z u_\tau}{\nu}\right)^{1/2}, \tag{4.4}$$

where we have used the dissipation scaling in (2.4) to relate τ_η to the vertical coordinate, z. This relationship indicates that both particle inertia and gravity have an explicit role, and an implicit role (through E) to play in potential non-local effects.

We know from Good *et al.* (2014) and Loth (2023) that in small scale laboratory experiments, $E \sim 0.2$ as St_η and Sv_ℓ approach unity, but as both of these parameters increase, E tends back towards zero, and may even become negative (Ferran *et al.* 2023). Therefore, for the coarse particles we are concerned with in this work, we can make a locally homogeneous approximation when $St_\eta Sv_\ell \ll (z u_\tau/\nu)^{1/2}$. This may not particularly restrictive for the atmospheric surface layer as the Reynolds numbers are $O(10^6)$, but for laboratory experiments, the integral scales tend to scale with the size of the experimental domain (i.e. $z \sim h$ where h could be the half-height of a channel). This could present a problem making a locally homogeneous approximation for coarse particles in a wind tunnel set-up.

For the DNS presented in this work, the above relationship shows that non-local effects are likely only important for cases when both St^+ and Sv^+ are large, as Sv_ℓ tends to scale with Sv^+ since $u' \sim u_\tau$. For example, if we consider cases with $St^+ = 100$ and $Sv^+ = 2.5$ (and assume $E \approx 0$), we can see immediately that (4.4) is not satisfied. This may explain the differences between the DNS and the model in Berk & Coletti (2021) in figures 6(*a*) and 6(*b*) for these particles. One of the main conclusions of this work is that for the governing continuum equation for the particle slip velocity in a TBL, there are tendencies that arise due to the inhomogeneities in the turbulence associated with the presence of the wall and the fact that the particle settling velocity is non-zero. However, as we have shown, for moderately sized particles (characterized by St^+ or St_η), and $Sv^+ < 1$, these terms are subleading outside of the viscous sublayer. Moreover, the magnitudes of these terms in the logarithmic layer tend to diminish as Re_τ increases. Thus, outside of the

viscous sublayer, and at moderate local St_η and Sv^+, we can extend models designed for homogeneous turbulence (like that described in Berk & Coletti (2021)) to a TBL, where we must interpret the model as local to a height z. However, outside of this regime (i.e. for very large and strongly settling particles), there are implicit non-local effects that appear as particles tend to settle through the flow due to the vertical variation of the turbulent statistics along the particle trajectories.

4.2. *Implications for modelling coarse particle transport in the atmospheric surface layer*

Interpreting DNS results in terms of the laboratory or field scales must be done with care, as the Reynolds numbers in DNS numbers are much smaller than those found at these scales. However, by scaling up the results in this work, we can gain valuable qualitative insights into the drag on inertial settling dust particles. For example, using estimates of turbulent dissipation for an atmospheric surface layer of roughly 10^{-3} m^2 s^{-3}, we can define a rough Kolmogorov time scale as 10^{-1} s. Thus, for quartz dust particles ($\rho_p = 2650$ kg m^{-3}) that range between 30–100 μm, we should expect a value of St_η to range between 0.1–10. We can see that the ranges in our DNS are in the correct neighbourhood to model these same coarse dust particles. Moreover, we can use the values of g^+ from table 1 (recall $g^+ = Sv^+/St^+$) to estimate an equivalent friction velocity, u_τ^* (note that since we are rescaling, u_τ^* is necessarily different than the value of u_τ used in this work), which effectively gives us a qualitative estimate of the intensity of the turbulence in an atmospheric surface layer. The effective friction velocity is given by

$$u_\tau^* = \left(\frac{g\nu}{g^+}\right)^{1/3}. \tag{4.5}$$

Assuming $g = 9.81$ m s^{-2} and $\nu = 1.57 \times 10^{-5}$ m^2 s^{-1}, and some relationship between 10 m wind velocity and the friction velocity (see Kantha & Clayson (2000) for example), this gives us a proxy for wind speed at the field scale. For the values of g^+ in this manuscript (see table 1), the effective friction velocities vary between 0.09 m s^{-1} and 0.84 m s^{-1}, which covers a wide range of friction velocities on the Earth (Vickers, Mahrt & Andreas 2015). Since g^+ is proportional to Sv^+, we can see the effective wind speed increases as Sv^+ decreases.

Therefore, the insight we can gain is that the slip velocity in high wind conditions (small Sv^+) should be primarily governed by the fluctuations associated with the turbulence, as opposed to the mean induced by gravitational settling and the presence of the solid boundary. Conversely, at lower wind speeds, the drag induced by turbulent fluctuations is much smaller relative to the mean slip. Thus, the magnitude of the slip velocity should instead be controlled by the average, which itself is controlled by the Stokes settling velocity and the turbophoretic term. Likewise, we expect the higher moment terms governing the slip variance (i.e. R_t and R_g) to be more important to the dynamics farther away from the surface in this limit, relatively speaking.

This is significant when applying models like BC2021 to particle transport in field scale systems. For example, as we have described previously, BC2021 can be used (in conjunction with a model for the unconditional fluid velocity variance) to predict the slip velocity variance for inertial settling particles in homogeneous turbulence. Under low Sv^+ conditions, our results show that the magnitude of the slip velocity is primarily governed by its fluctuating component, which is in turn associated with the interactions with the turbulence. Moreover, as we have discussed, a locally homogeneous approximation may be used when Sv^+ is small enough (see (4.4)), our work suggests that BC2021 can

also be applied to inhomogeneous turbulence, like that of the atmospheric surface layer, provided we are not concerned with dynamics too close to the ground and the wind conditions are strong enough. Another interesting related application is towards modelling the particle Reynolds number, which is known to affect the associated drag on the particles (Balachandar 2009; Berk & Coletti 2024). For example, it is known that loitering effects are typically associated with large particle Reynolds number (Rosa *et al.* 2016), and these loitering effects work to reduce the average particle settling velocity (Good *et al.* 2014). Accurate modelling of loitering effects could explain discrepancies between numerical simulations and laboratory experiments with respect to the measurement of settling velocities (Ferran *et al.* 2023). Moreover, our results may gain some insights into further than expected horizontal transport of giant dust particles off of the West African coast (Van Der Does *et al.* 2018), which could be linked to loitering effects.

Funding. The authors would like to acknowledge grant no. W911NF2220222 from the U.S. Army Research Office. The authors would also like to thank the Center for Research Computing at the University of Notre Dame, and the three anonymous reviewers whose comments have increased the overall quality of the work.

Declaration of interests. The authors report no conflict of interest.

Appendix A. Mathematical details of slip velocity model hierarchy

By including gravitational settling in the particle equation of motion, there is now a mean settling velocity. Due to preferential sweeping, the average particle settling velocity can be increased (or decreased in some cases) beyond the laminar settling velocity, v_g, leading to there is a non-zero average slip velocity. Since we know that the average settling velocity of the particles will be non-zero due to the presence of gravity, the average of the square is not equivalent to the variance, i.e. $\langle F^2\rangle \neq \langle F'^2\rangle$, ($F$ is some arbitrary quantity, and a prime indicates a fluctuation about the mean of F) meaning we must be careful to discern between the variance and squared means,

$$\langle w_p^2\rangle_z = \langle w_p\rangle_z^2 + \langle {w_p'}^2\rangle_z, \tag{A1}$$

$$\langle w_s^2\rangle_z = \langle w_s\rangle_z^2 + \langle {w_s'}^2\rangle_z, \quad \langle w_s\rangle_z = \langle w_f\rangle_z - \langle w_p\rangle_z, \tag{A2}$$

$$\langle w_p^3\rangle_z = \langle w_p\rangle_z^3 + \langle w_p\rangle_z\langle {w_p'}^2\rangle_z + \langle {w_p'}^3\rangle_z. \tag{A3}$$

Equation (2.17), derived in Johnson *et al.* (2020), assumed that particles did not settle under the action of gravity, meaning that $\langle w_p\rangle_z = 0$. However, by substituting in the above Reynolds decompositions, it can be readily extended to settling particles. Doing this, we arrive at

$$\langle {w_s'}^2\rangle_z = \langle {w_f'}^2\rangle_z - \langle {w_p'}^2\rangle_z - \frac{\tau_p}{\varrho}\frac{d}{\mathrm{d}z}\varrho\langle w_p^3\rangle_z + \langle w_f\rangle_z^2 - \langle w_s\rangle_z^2 - \langle w_p\rangle_z^2 - 2\langle w_p\rangle_z v_g, \tag{A4}$$

where we have not expanded $\langle w_p^3\rangle_z$ in terms of its variance and mean components yet. We can see from this equation that the slip velocity variance is due to the variance of seen velocities, the variance of the particle velocity, and several other terms. These terms are difficult to interpret in their current form, so we simplify them next.

The mean slip velocity squared, $\langle w_s\rangle_z^2$ can be expanded as

$$\langle w_s\rangle_z^2 = \langle w_f\rangle_z^2 - 2\langle w_f\rangle_z\langle w_p\rangle_z + \langle w_p\rangle_z^2. \tag{A5}$$

Upon substitution of the above into (A4) and simplifying, we can express (A4) as

$$\langle w_s'^2\rangle_z = \langle w_f'^2\rangle_z - \langle w_p'^2\rangle_z - \frac{\tau_p}{\varrho}\frac{d}{\mathrm{d}z}\varrho\langle w_p^3\rangle_z + 2\langle w_p\rangle_z\left(\langle w_s\rangle_z - v_g\right). \tag{A6}$$

We can now expand the third term on the right-hand side of the above in order to express the slip velocity variance in terms of only means and variances of other quantities,

$$\langle w_s'^2\rangle_z = \overbrace{\underbrace{\langle w_f'^2\rangle_z - \langle w_p'^2\rangle_z}_{(1)} - \frac{\tau_p}{\varrho}\frac{d}{\mathrm{d}z}\varrho\langle w_p'^3\rangle_z}^{(2)}$$
$$\underbrace{-\frac{\tau_p}{\varrho}\frac{d}{\mathrm{d}z}(\varrho\langle w_p\rangle_z^3 + 3\varrho\langle w_p\rangle_z\langle w_p'^2\rangle_z) + 2\langle w_p\rangle_z\left(\langle w_s\rangle_z - v_g\right)}_{(3)}. \tag{A7}$$

Appendix B. Comparison of computed and modelled slip variance

Figure 7(*a*) shows a comparison between computed values of $\langle w_s'^2\rangle_z$ and that computed using the right-hand side of (2.18). The slip variance computed directly from the DNS for three different values of Sv^+ at $St^+ = 10$ are shown by black curves, while the right-hand side of (2.18) are shown by coloured dashed lines. We can see that the right-hand side contains significant noise, but otherwise models the computed slip variance well. This noise is a result of the routines used to estimate the derivatives in R_t and R_g, and not in the computation of $\langle w_f'^2\rangle_z$ and $\langle w_p'^2\rangle_z$ (as evidenced in figure 2). Figure 7(*b*) shows a comparison between the computed values of $R_t + R_g$ (dashed curves) and that computed by a residual of (2.18) (black solid curves). We can see that by plotting R_t and R_g as a residual, the noise is significantly reduced.

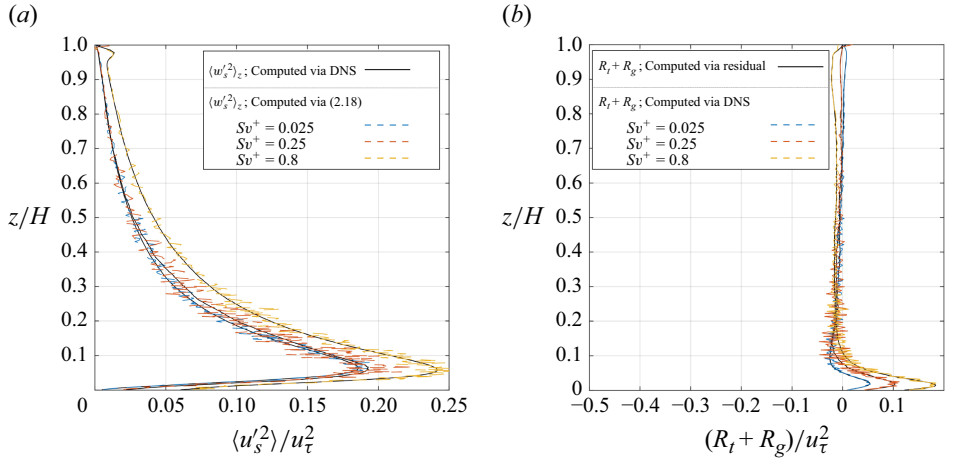

Figure 7. Panel (*a*) shows the slip velocity variance computed by the DNS for three values of Sv^+ at fixed $St^+ = 10$ (black curves), and the slip variance computed by (2.18) (dashed coloured curves). Panel (*b*) shows $R_t + R_g$ computed via a residual of $\langle w_s'\rangle_z - (\langle w_f'\rangle_z - \langle w_p'\rangle_z)$ (black curves), and $R_t + R_g$ computed directly (dashed coloured curves) for the same cases.

Appendix C. Response function model of acceleration variance

In this section, we sketch the derivation of the semianalytical model proposed by Berk & Coletti (2021) for the slip velocity variance. The following is based on the concept of a response function, described in Csanady (1963), which is meant to quantify the fact that inertial particles require a finite amount of time to respond to turbulent fluctuations. By Fourier-transforming the vertical component of the fluctuating particle velocity and the sampled velocity through the use of standard manipulations, we can write the slip velocity variance and the particle velocity variance as

$$\langle {w_s'}^2 \rangle = \int_0^\infty (\omega\tau_p)^2 E_p \, \mathrm{d}\omega, \quad \langle {w_p'}^2 \rangle = \int_0^\infty E_p \, \mathrm{d}\omega. \tag{C1}$$

In this equation, E_p is the kinetic energy spectrum of the particles. As discussed in Csanady (1963), E_p is related to the kinetic energy spectrum of the fluid motion sampled along the particle's trajectory, denoted by $E_{f,p}$, through a response function

$$H(\omega) = \frac{1}{1 + (\omega\tau_p)^2}, \tag{C2}$$

meaning that

$$\langle {w_s'}^2 \rangle = \int_0^\infty (\omega\tau_p)^2 H(\omega) E_{f,p} \, \mathrm{d}\omega, \quad \langle {w_p'}^2 \rangle = \int_0^\infty H(\omega) E_{f,p} \, \mathrm{d}\omega. \tag{C3}$$

Using the stochastic model for the particle velocity autocorrelation outlined in Sawford (1991), Berk & Coletti (2021) used the fact that the autocorrelation and the spectra are Fourier transform pairs. The particle velocity autocorrelation described in Sawford (1991) is

$$R_{f,p}(t) = \frac{\langle {w_f'}^2 \rangle}{\tau_{l,p} - \tau_2} \left(\tau_{l,p} e^{-t/\tau_{l,p}} + \tau_2 e^{-t/\tau_2} \right), \tag{C4}$$

where τ_2 is proportional to the fluid acceleration variance and appears due to the finite Reynolds number. For this work, we use

$$\tau_2 = \frac{C_0}{2a_0} \tau_\eta, \tag{C5}$$

where C_0 and a_0 are universal constants modelled by

$$C_0 = C_\infty (1 - (0.1 {Re_\lambda}^{-1/2})), \quad a_0 = \left(\frac{5}{1 + 110 Re_\lambda^{-1}} \right), \tag{C6}$$

defined in Lien & D'Asaro (2002) and Sawford *et al.* (2003), respectively. Here, $Re_\lambda = \sqrt{15}\langle w^2 \rangle / v_\eta^2$ is the Taylor–Reynolds number evaluated at a height z. Thus, C_0 and a_0 are functions of the vertical coordinate. Note that the results in this work are not meaningfully dependent on the exact choice of model for C_0 and a_0.

Here $\tau_{l,p}$ is the Lagrangian correlation time scale of the turbulence along the particle trajectory. Here $\tau_{l,p}$ is a function of three parameters: ratio of the laminar settling velocity to the integral velocity scale; the Lagrangian correlation time scale of the turbulence; the Eulerian correlation time scale of the turbulence which are defined as

$$Sv_\ell = \frac{v_g}{w'}, \quad \tau_E = \frac{\langle w^2 \rangle}{\epsilon}, \quad \tau = -\frac{\kappa z}{u_\tau} \frac{\langle uw \rangle}{\langle w^2 \rangle}, \tag{C7}$$

respectively. Note that the definition of τ can be found in Oesterlé & Zaichik (2004). Here $\tau_{l,p}$ is meant to encapsulate the fact that as an inertial particle settles through a local neighbourhood of correlated motion, the turbulence it experiences decorrelates faster along its trajectory than it would if it was not settling. Berk & Coletti (2021) derived a semiempirical model for the correlation along the particle trajectory using the idea of the crossing trajectories mechanism introduced by Csanady (1963) as

$$\tau_{l,p} = \tau \frac{1}{\left(1 + \left(\frac{\tau}{\tau_E}\right)^2 Sv_\ell^2\right)^{1/2}}. \tag{C8}$$

By Fourier-transforming $R_{f,p}$ and substituting into the integral relations for the slip variance and velocity variance, we arrive at the following for the velocity variance:

$$\langle {w'_p}^2 \rangle = \langle {w'_f}^2 \rangle \left(1 - \frac{St_\eta^2}{\left(St_\eta + \frac{\tau_{l,p}}{\tau_\eta}\right)\left(St_\eta + \frac{\tau_2}{\tau_\eta}\right)}\right), \tag{C9}$$

and the slip variance

$$\langle {w'_s}^2 \rangle = \langle {w'_f}^2 \rangle \frac{St_\eta^2}{\left(St_\eta + \frac{\tau_{l,p}}{\tau_\eta}\right)\left(St_\eta + \frac{\tau_2}{\tau_\eta}\right)}. \tag{C10}$$

If follows from the above that the particle acceleration variance is

$$\langle {a'_p}^2 \rangle = \langle {w'_f}^2 \rangle \frac{1}{\left(St_\eta + \frac{\tau_{l,p}}{\tau_\eta}\right)\left(St_\eta + \frac{\tau_2}{\tau_\eta}\right)}. \tag{C11}$$

Since the term in the brackets in (C9) is simply the model for $1 - \langle {w'_s}^2 \rangle / \langle {w'_f}^2 \rangle$, the implied relationship between the slip variance and the particle velocity variance is

$$\langle {w'_s}^2 \rangle = \langle {w'_f}^2 \rangle - \langle {w'_p}^2 \rangle, \tag{C12}$$

which is almost identical to (2.18), except for the fact that R_t and R_g are not accounted for in this model.

References

Adebiyi, A. *et al.* 2023 A review of coarse mineral dust in the Earth system. *Aeolian Res.* **60**, 100849.

Aliseda, A., Cartellier, A., Hainaux, F. & Lasheras, J.C. 2002 Effect of preferential concentration on the settling velocity of heavy particles in homogeneous isotropic turbulence. *J. Fluid Mech.* **468**, 77–105.

Arcen, B. & Tanière, A. 2009 Simulation of a particle-laden turbulent channel flow using an improved stochastic Lagrangian model. *Phys. Fluids* **21** (4), 043303.

Balachandar, S. 2009 A scaling analysis for point–particle approaches to turbulent multiphase flows. *Intl J. Multiphase Flow* **35** (9), 801–810.

Bec, J., Biferale, L., Boffetta, G., Celani, A., Cencini, M., Lanotte, A., Musacchio, S. & Toschi, F. 2006 Acceleration statistics of heavy particles in turbulence. *J. Fluid Mech.* **550**, 349.

Bec, J., Homann, H. & Ray, S.S. 2014 Gravity-driven enhancement of heavy particle clustering in turbulent flow. *Phys. Rev. Lett.* **112** (18), 184501.

Berk, T. & Coletti, F. 2020 Transport of inertial particles in high-Reynolds-number turbulent boundary layers. *J. Fluid Mech.* **903**, A18.

Berk, T. & Coletti, F. 2021 Dynamics of small heavy particles in homogeneous turbulence: a Lagrangian experimental study. *J. Fluid Mech.* **917**, A47.

Berk, T. & Coletti, F. 2023 Dynamics and scaling of particle streaks in high-Reynolds-number turbulent boundary layers. *J. Fluid Mech.* **975**, A47.

BERK, T. & COLETTI, F. 2024 An analytical model for the slip velocity of particles in turbulence. *J. Fluid Mech.* **996**, A1.

BRAGG, A.D., IRELAND, P.J. & COLLINS, L.R. 2015 On the relationship between the non-local clustering mechanism and preferential concentration. *J. Fluid Mech.* **780**, 327–343.

BRAGG, A.D., RICHTER, D.H. & WANG, G. 2021*a* Mechanisms governing the settling velocities and spatial distributions of inertial particles in wall-bounded turbulence. *Phys. Rev. Fluids* **6** (6), 064302.

BRAGG, A.D., RICHTER, D.H. & WANG, G. 2021*b* Settling strongly modifies particle concentrations in wall-bounded turbulent flows even when the settling parameter is asymptotically small. *Phys. Rev. Fluids* **6** (12), 124301.

BRANDT, L. & COLETTI, F. 2022 Particle-laden turbulence: progress and perspectives. *Annu. Rev. Fluid Mech.* **54** (1), 159–189.

COSTA, P., BRANDT, L. & PICANO, F. 2020 Interface-resolved simulations of small inertial particles in turbulent channel flow – CORRIGENDUM. *J. Fluid Mech.* **891**, E2.

VAN DER DOES, M., KNIPPERTZ, P., ZSCHENDERLEIN, P., GILES HARRISON, R. & STUUT, J.-B.W. 2018 The mysterious long-range transport of giant mineral dust particles. *Sci. Adv.* **4** (12), eaau2768.

CSANADY, G.T. 1963 Turbulent diffusion of heavy particles in the atmosphere. *J. Atmos. Sci.* **20** (3), 201–208.

FERRAN, A., MACHICOANE, N., ALISEDA, A. & OBLIGADO, M. 2023 An experimental study on the settling velocity of inertial particles in different homogeneous isotropic turbulent flows. *J. Fluid Mech.* **970**, A23.

GAO, W., SAMTANEY, R. & RICHTER, D.H. 2023 Direct numerical simulation of particle-laden flow in an open channel at. *J. Fluid Mech.* **957**, A3.

GERASHCHENKO, S., SHARP, N.S., NEUSCAMMAN, S. & WARHAFT, Z. 2008 Lagrangian measurements of inertial particle accelerations in a turbulent boundary layer. *J. Fluid Mech.* **617**, 255–281.

GOOD, G.H., IRELAND, P.J., BEWLEY, G.P., BODENSCHATZ, E., COLLINS, L.R. & WARHAFT, Z. 2014 Settling regimes of inertial particles in isotropic turbulence. *J. Fluid Mech.* **759**, R3.

GRACE, A.P., RICHTER, D.H. & BRAGG, A.D. 2024 A reinterpretation of phenomenological modeling approaches for lagrangian particles settling in a turbulent boundary layer. *Boundary-Layer Meteorol.* **190** (4), 15.

IRELAND, P.J., BRAGG, A.D. & COLLINS, L.R. 2016*a* The effect of Reynolds number on inertial particle dynamics in isotropic turbulence. Part 1. Simulations without gravitational effects. *J. Fluid Mech.* **796**, 617–658.

IRELAND, P.J., BRAGG, A.D. & COLLINS, L.R. 2016*b* The effect of Reynolds number on inertial particle dynamics in isotropic turbulence. Part 2. Simulations with gravitational effects. *J. Fluid Mech.* **796**, 659–711.

JOHNSON, P.L., BASSENNE, M. & MOIN, P. 2020 Turbophoresis of small inertial particles: theoretical considerations and application to wall-modelled large-eddy simulations. *J. Fluid Mech.* **883**, A27.

KANTHA, L.H. & CLAYSON, C.A. 2000 *Small Scale Processes in Geophysical Fluid Flows*. Elsevier.

KOK, J.F. 2011 A scaling theory for the size distribution of emitted dust aerosols suggests climate models underestimate the size of the global dust cycle. *Proc. Natl Acad. Sci. USA* **108** (3), 1016–1021.

KOK, J.F., PARTELI, E.J.R., MICHAELS, T.I. & KARAM, D.B. 2012 The physics of wind-blown sand and dust. *Rep. Prog. Phys.* **75** (10), 106901.

KOK, J.F., STORELVMO, T., KARYDIS, V.A., ADEBIYI, A.A., MAHOWALD, N.M., EVAN, A.T., HE, C. & LEUNG, D.M. 2023 Mineral dust aerosol impacts on global climate and climate change. *Nat. Rev. Earth Environ.* **4** (2), 71–86.

KUNKEL, G.J. & MARUSIC, I. 2006 Study of the near-wall-turbulent region of the high Reynolds-number boundary layer using an atmospheric flow. *J. Fluid Mech.* **548**(-1), 375–402.

LAVEZZO, V., SOLDATI, A., GERASHCHENKO, S., WARHAFT, Z. & COLLINS, L.R. 2010 On the role of gravity and shear on inertial particle accelerations in near-wall turbulence. *J. Fluid Mech.* **658**, 229–246.

LEE, J. & LEE, C. 2019 The effect of wall-normal gravity on particle-laden near-wall turbulence. *J. Fluid Mech.* **873**, 475–507.

LIEN, R.-C. & D'ASARO, E.A. 2002 The Kolmogorov constant for the Lagrangian velocity spectrum and structure function. *Phys. Fluids* **14** (12), 4456–4459.

LOTH, E. 2023 Particles in a turbulent gas: diffusion, bias, modulation and collisions. *Prog. Energy Combust.* **97**, 101094.

MARCHIOLI, C., SOLDATI, A., KUERTEN, J.G.M., ARCEN, B., TANIÈRE, A., GOLDENSOPH, G., SQUIRES, K.D., CARGNELUTTI, M.F. & PORTELA, L.M. 2008 Statistics of particle dispersion in direct numerical simulations of wall-bounded turbulence: results of an international collaborative benchmark test. *Intl J. Multiphase Flow* **34** (9), 879–893.

MAXEY, M.R. & RILEY, J.J. 1983 Equation of motion for a small rigid sphere in a nonuniform flow. *Phys. Fluids* **26** (4), 883–889.

MENG, J., HUANG, Y., LEUNG, D.M., LI, L., ADEBIYI, A.A., RYDER, C.L., MAHOWALD, N.M. & KOK, J.F. 2022 Improved parameterization for the size distribution of emitted dust aerosols reduces model underestimation of super coarse dust. *Geophys. Res. Lett.* **49** (8), e2021GL097287.

MINIER, J.-P. & PEIRANO, E. 2001 *The Pdf Approach to Turbulent Polydispersed Two-Phase Ows*. Physics Reports.

MORA, D.O., OBLIGADO, M., ALISEDA, A. & CARTELLIER, A. 2021 Effect of Re 03BB; and Rouse numbers on the settling of inertial droplets in homogeneous isotropic turbulence. *Phys. Rev. Fluids* **6** (4), 044305.

OESTERLÉ, B. & ZAICHIK, L.I. 2004 On Lagrangian time scales and particle dispersion modeling in equilibrium turbulent shear flows. *Phys. Fluids* **16** (9), 3374–3384.

POZORSKI, J. & MINIER, J.-P. 1998 On the Lagrangian turbulent dispersion models based on the Langevin equation. *Intl J. Multiphase Flow* **24** (6), 913–945.

RICHTER, D. & CHAMECKI, M. 2018 Inertial effects on the vertical transport of suspended particles in a turbulent boundary layer. *Boundary-Layer Meteorol.* **167** (2), 235–256.

RICHTER, D.H. & SULLIVAN, P.P. 2013 Momentum transfer in a turbulent, particle-laden Couette flow. *Phys. Fluids* **25** (5), 053304.

ROSA, B., PARISHANI, H., AYALA, O. & WANG, L.-P. 2016 Settling velocity of small inertial particles in homogeneous isotropic turbulence from high-resolution DNS. *Intl J. Multiphase Flow* **83**, 217–231.

ROSENBERG, P.D. *et al.* 2014 Quantifying particle size and turbulent scale dependence of dust flux in the sahara using aircraft measurements: AIRCRAFT MEASUREMENTS OF DUST FLUX. *J. Geophys. Res.: Atmos.* **119** (12), 7577–7598.

RYDER, C.L., HIGHWOOD, E.J., WALSER, A., SEIBERT, P., PHILIPP, A. & WEINZIERL, B. 2019 Coarse and giant particles are ubiquitous in Saharan dust export regions and are radiatively significant over the Sahara. *Atmos. Chem. Phys.* **19** (24), 15353–15376.

RYDER, C.L. *et al.* 2018 Coarse-mode mineral dust size distributions, composition and optical properties from AER-d aircraft measurements over the tropical eastern Atlantic. *Atmos. Chem. Phys.* **18** (23), 17225–17257.

SAWFORD, B.L. 1991 Reynolds number effects in Lagrangian stochastic models of turbulent dispersion. *Phys. Fluids A: Fluid Dyn.* **3** (6), 1577–1586.

SAWFORD, B.L., YEUNG, P.K., BORGAS, M.S., VEDULA, P., LA PORTA, A., CRAWFORD, A.M. & BODENSCHATZ, E. 2003 Conditional and unconditional acceleration statistics in turbulence. *Phys. Fluids* **15** (11), 3478–3489.

SHAO, Y. 2008 Dust transport and deposition. In *Physics and Modelling of Wind Erosion*, pp. 247–301, Springer Netherlands.

SMITS, A.J., MCKEON, B.J. & MARUSIC, I. 2011 High–Reynolds number wall turbulence. *Annu. Rev. Fluid Mech.* **43** (1), 353–375.

TOM, J. & BRAGG, A.D. 2019 Multiscale preferential sweeping of particles settling in turbulence. *J. Fluid Mech.* **871**, 244–270.

VICKERS, D., MAHRT, L. & ANDREAS, E.L. 2015 Formulation of the sea surface friction velocity in terms of the mean wind and bulk stability. *J. Appl. Meteorol. Clim.* **54** (3), 691–703.

WANG, G., FONG, K.O., COLETTI, F., CAPECELATRO, J. & RICHTER, D.H. 2019 Inertial particle velocity and distribution in vertical turbulent channel flow: a numerical and experimental comparison. *Intl J. Multiphase Flow* **120**, 103105.

WANG, L.-P. & STOCK, D.E. 1993 Dispersion of heavy particles by turbulent motion. *J. Atmos. Sci.* **50** (13), 1897–1913.

YEO, K., KIM, B.-G. & LEE, C. 2010 On the near-wall characteristics of acceleration in turbulence. *J. Fluid Mech.* **659**, 405–419.

YUDINE, M.I. 1959 Physical considerations on heavy-particle diffusion. *Adv. Geophys.* **6**, 185–191.

ZAMANSKY, R., VINKOVIC, I. & GOROKHOVSKI, M. 2011 Acceleration statistics of solid particles in turbulent channel flow. *Phys. Fluids* **23** (11), 113304.

ZHANG, Y., BRAGG, A.D. & WANG, G. 2023 Asymptotic closure model for inertial particle transport in turbulent boundary layers. *Phys. Rev. Fluids* **8** (1), 014301.